# Chapter 9

# Size- and Shape-Controlled Hybrid Inorganic Nanomaterials and Application for Low-Temperature CO Oxidation

**Thanh-Dinh Nguyen and Trong-On Do***
*Department of Chemical Engineering, Laval University, Quebec G1V 0A6, Canada*
*Trong-On.Do@gch.ulaval.ca

This chapter is focused on the recent strategies developed to create multicomponent dumbbell and core–shell nanohybrids that yielded from the combination of different single-nanoscale components via seed-mediated methods. Further controlling the heterogeneous growth of multicomponent nuclei by adjusting the synthetic parameters, leading to the desired morphology of the final dumbbells and core–shells nanohybrid products is discussed. Nanohybrids with their unique features and multifunctional properties due to the interplay between their structure, morphology, and composition are briefly presented. The catalytic activity of these nanohybrids for low temperature CO catalytic oxidation is also highlighted.

---

*Controlled Nanofabrication: Advances and Applications*
Edited by Ru-Shi Liu

ISBN 978-981-4316-87-3 (Hardcover), 978-981-4364-51-5 (eBook)
www.panstanford.com

## 9.1 Introduction

Hybrid inorganic nanomaterials are elaborated multicomponent nanocrystals (NCs), consisting of two or more different single nanocomponents that are permanently joint through chemical-bonding interfaces with or without any molecular bridges, eventually attaining hetero-epitaxial junctions. In the past decades, hybrid inorganic nanomaterials have attracted considerable research attention because an hybrid system can usually provide new collective properties, which are not available from the corresponding individual components [1]. They possess not only the multifunctionalities but also unique features arising from the particle–particle interactions, as well as intricate phase-segregated hetero-architectures made of discrete-shaped sections fused via small connecting areas at selected locations [2, 3]. The combination of multiple components into a single colloidal particle at the nanoscale can be achieved through the permanent inorganic interface, where each side of particle in the hybrid system is restricted to the nanoscale junction. The particle-particle interactions could allow the electron transport across the interface that changes the local electronic structure and induces the synergetic properties of the nanohybrids [4, 5]. The physiochemical properties of hybrid nanostructures can be finely tuned and optimized by controlling the geometries, their composition of each component, and interfacial interactions as well as incorporation of metals onto nanosupports. For example, the peculiar optical and/or conduction behavior observable for nanohybrids based on semiconductors and noble metals can result from altered quantum confinement degree, modified charge-carrier recombination or separation dynamics, and/or plasmon-to-exciton coupling effects. It is known that metal clusters deposited on the nanocrystal surface acts as sinks for transferring the electron from support surface to reagents to perform the oxidation/redox processes [6]. The charge distribution between metal and support thus plays an important role in improving the catalytic activity [7]. As a result, such hybrid nanomaterials have highlighted the featured properties for the various potential applications in catalysts, optical devices, solar energy conversions, magnetic-resonance-imaging (MRI) agents, chemical sensors [8, 9], that go beyond those of the individual component. The synthesis of colloidal nanohybrids requires developing a higher degree of synthetic ingenuity and creativity. The conjugation of the single components forming the hybrid nanoarchitectures typically occurs at the critical thermodynamic-kinetic crossovers through atomic diffusion, ionic exchange, specific facet reactivity, and/or interfacial strain. The large surface-to-weight ratio and the quantum size effect of the metal particles inherent in the nanohybrid system have impacted the critical factors that could be affected their desired performances. The unique properties of the nanohybrids are mostly dependent on the morphological structure associated with their interface area and density of active sites [10]. For example, the Banin's group had successfully achieved the growth of noble metal nanodots on one or two tips of semiconductor nanorods [4]. The exposed facets on the semiconductor tips were considered direct electrical contact points and assembling and reaction centers.

The seed-mediated growth protocols, including thermal decomposition, micro emulsion, hydro/solvothermal process, etc., to prepare single-nanocomponents in the solution phase have been extended to multicomponent nanocrystals such as metal oxide, metal semiconductor, metal–metal species [10, 11]. Colloidal nanohybrids are generated upon reaction of molecular precursors in a liquid solution and tailored with sub-nanometer-level accuracy over a broad range of dimensional morphological regimes by careful regulation of critical thermodynamic parameters and growth kinetics in liquid media under assistance of selected coordinating solvents, surfactants, or catalyst additives. The organic capping agents, as stabilizers, play several key roles along the course of the nanohybrid formation. Such stabilizers would regulate the solution supersaturation degree upon forming complexes with the monomers and participate in an adsorption–desorption equilibrium at the surface of the growing clusters, preventing irreversible aggregation and ensuring steady growth advancement. In general, the nanohybrids with representative dumbbell or core–shell shapes are obtained by sequential growth of a second component on preformed seeds with or without linker molecules through the directed attachment. In the growth process for hybrid nanomaterials, the dumbbell-shaped nanohybrids are formed from two components having the similar lattice spacings; while the lattice mismatches often lead to generate the core–shell structure [12]. These points suggest that the selection of suitable-structured elements is critical for the designed hybrid nanostructures relative to the electron-transferred capacity at the interface of two components. Therefore, the flexible combination of evolved synthetic control along with the understanding of size/shape-, crystal-phase, interface-dependent properties of the constituent building units via engineering their relative spatial arrangement and relevant interface structure have already opened up several avenues of diverse new applications. A general picture in Fig. 9.1 is schematically illustrated for the shape-controlled features and practical applications of the hybrid materials at the nanoscale.

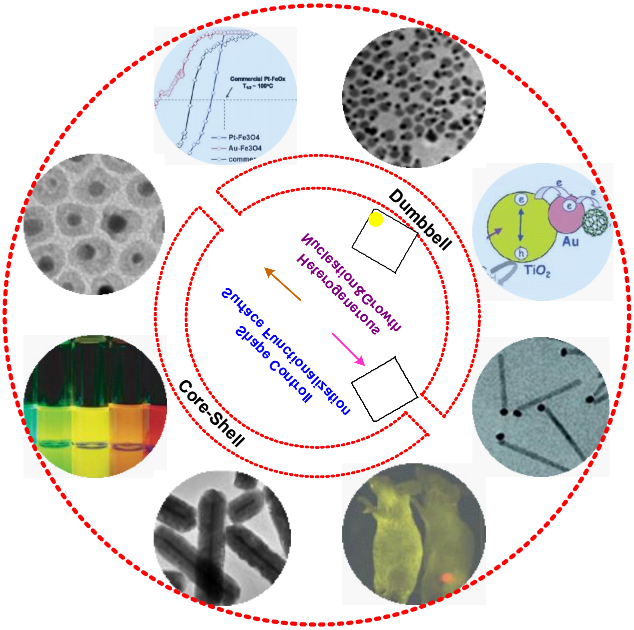

**Figure 9.1** The conceptual generation, shape control, and surface functionalization of the various types of conjugated inorganic nanohybrids using as key building blocks for the yield of novel functional nanodevices for catalytic, electronic, optical, and biomedical technologies.

The oxidation of carbon monoxide is one of the pivotal reactions in heterogeneous catalysis, owing to its application in indoor air cleaning and toxic pollutant treatment from automobile exhaust [13, 14]. Nanocrystals of metal, metal oxide, mixed oxide, hybrid metal-oxide species are attractive for use as heterogeneous catalysts for low-temperature CO oxidation reactions during the past decade because of their high surface-to-volume ratios and high surface energies [15, 16]. The high surface area of nanocatalyst would yield a number of defect sites that are coordinatively unsaturated ions or surface atoms arising from planes, edges, corners, anion/cation vacancies, and electron excess centers [17]. Such defect sites are often attributed as the active sites for many useful and interesting catalytic reactions. It has been demonstrated that morphology effects appear for catalytic reactions that are structural sensitive [18, 19]. Both the size and shape of the nanocrystals determining the number of atoms located at the edges/corners are critical parameters that must be controlled to maximize their catalytic activity [20]. In addition, the surface atoms can occupy the corners and edges of the nanocrystals and thus become chemically unsaturated and also much more active. The high-index facets of inorganic single crystals often have a greater density of unsaturated atomic steps, ledges, and kinks, which can serve as active sites for the enhanced catalytic activity and selectivity [21, 22].

Recently, hybrid metal/oxide nanostructures as novel active catalysts with positional and shape control of the components have been viewed as promising candidates for low-temperature CO oxidation. In order to gain high catalytic activity, small-sized metal clusters have generally to well disperse onto the oxide support with the exposed high-energy facets [22, 23].

The emerging properties of the hybrid structures attributed to the interfacial particle-particle interactions have been proposed to originate from the contributions: (i) the presence of low coordinative metal sites; (ii) charge transfer between deposited species and supports; (iii) quantum size effects. Recent attempts have utilized the oxide nanocrystals as a support for the mutual dispersion of metal particles. In general, two main routes have typically been used for the controlled growth of metal-oxide nanohybrids: (i) light-induced growth of the metal onto the pre-synthesized oxide-semiconductor nanocrystals and (ii) reduced solution reaction of metal salt on the functionalized-oxide nanocrystals [24]. Considerable progress in analytical characterization has also contributed to a better understanding of the particle–particle interactions and catalytic activity. In this review, the catalytic CO oxidation activity of colloidal hybrid metal@oxide nanocrystals with various shapes and components synthesized by various surfactant-assisted methods will also be presented.

## 9.2 Concepts in Surfactant-Assisted Synthesis of Multicomponent Nanohybrids

Colloidal nanohybrids are generated upon reaction of molecular precursors in a liquid solution in the presence of surfactant agents. Once the synthesis is activated at a suitable temperature, the monomers are generated and then induce the nucleation of nanocrystals and sustain their subsequent enlargement. The organic surfactants play several key roles along the course of hybrid nanocrystal formation. Figure 9.2 shows the general seeded growth models for the fabrication of dumbbell- and core/shell-shaped hybrid nanocrystals, accordingly, it can be classified into five main synthetic approaches: (i) direct heterogeneous nucleation and growth of the metal precursors onto the surfaces (facet sites or tips) of preformed seeds (Fig. 9.2a–c); (ii) the small metal nanoparticles adsorb onto the opposite-charged surface of nanosupports by the photo-irradiation (Fig. 9.2d); (iii) reduced precipitated onto the colloidal nano-islands by the reduced reaction of the metal salt precursors previously adsorbed on their hydrophilic surface through ion exchange (Fig. 9.2e); (iv) metal precursor growth after chemical activation of the surface of nanosupports (Fig. 9.2f) ; (v) one-pot approaches by self-controlled nucleation growth (Fig. 9.2g). Following these pathways, a large variety of nano-hybrids, including metal oxide, metal semiconductor, metal–metal structures, has been successively synthesized (see below).

Understanding of the growth behavior and the morphology evolution is crucial for efficient synthesis and shape/size control of inorganic nanocrystals. Among the nanostructures, single-crystalline nanocrystals have received much attention. Appreciative adjustment of experimental parameters, such as the reaction temperature and time, the type and the concentrations of precursors and capping agents, and solvents, affects the crystal formation.

In the bottom-up syntheses, for the growth process of nuclei in the super-saturation solution upon forming complexes with the monomers, the behavior is described by the classical Ostwald ripening mechanism [17, 18], in which the growth of larger particles at the expense of smaller ones is driven by surface energy reduction. This phenomenon was extensively used to explain the formation of thermodynamically stable nanocrystals with nearly spherical morphologies. Systematic size tuning along with size-distribution narrowing can be achieved by balancing the relative consumption of monomers between the nucleation and the growth stages.

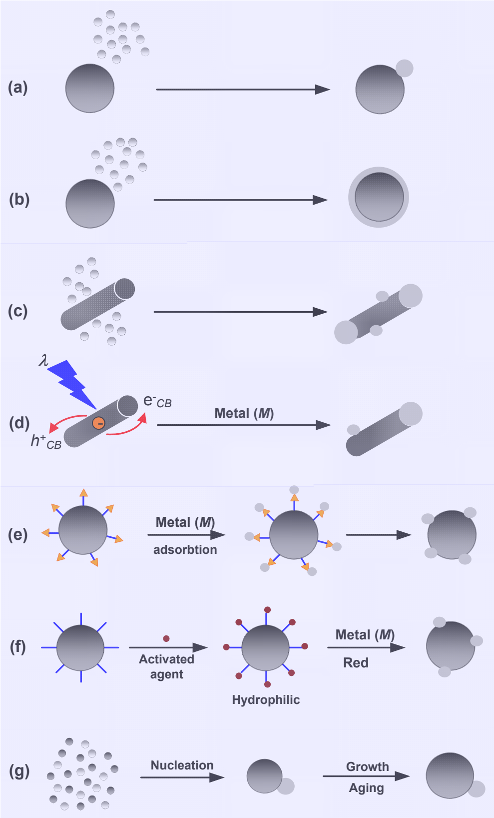

**Figure 9.2** Sketch of reaction mechanisms for the formation of hybrid nanocrystals: (a–c) direct heterogeneous nucleation and growth of the metal precursors onto the preformed seed surfaces; (d) metal particles adsorb onto the opposite-charged-surfaced nanosupports by the photo-irradiation; (e) redox-precipitation of metal precursors on the hydrophilic-surfaced nano-islands; (f) metal precursor growth on the activated-surfaced nanosupports; (g) one-pot approaches by self-controlled nucleation growth.

For the controlled self-assembly of nanoparticles into well-defined anisotropic nanostructures, organic capping reagents usually play critical roles in reducing the activity of the nanocrystal surface to promote or tune the ordered self-assembly. An oriented attachment mechanism could offer as an additional tool to design advanced materials with anisotropic properties and could be used for the synthesis of more complex crystalline one-dimensional structures. In addition, the sterically diffusive kinetics and selective binding or nonbinding of surfactant molecules to different faces of the growing nanocrystal can also control the product's morphology due to the possibility of breaking the limitations of crystal growth dynamically [19–23]. In some cases, the formation of the intrinsic anisotropic nanocrystals is found to be a highly kinetics-driven process, which occurs far away from the thermodynamic equilibrium and must be overdriven by high precursor monomer concentrations [24]. In the following sections, we present different types of the representative hybrid inorganic nanocrystals obtained from the capping agent-assisted methods: metal oxide in Section 9.1, metal semiconductor in Section 9.2, and metal–metal in Section 9.3, along with the discussion of the synthetic pathways of these nanomaterials and their corresponding formation mechanism and followed by the examples of CO catalytic activity in Section 9.4.

## 9.3 Types of Hybrid Inorganic Nanocrystals

### 9.3.1 Metal@Oxide

The properties of metal/oxide nanocrystals depend strongly on the nature of metal/oxide interfaces, the structure, morphology, and composition. A detailed insight into interfacial chemical/physical properties would thus deliver significant advantages from both a fundamental and an applicative point of view.

For example, iron-oxide-based materials are being studied intensively because of their potential as MRI agents. Au–$Fe_3O_4$ core–shell and dumbbell-shaped nanohybrids have shown enhanced optical, magnetic, and catalytic properties compared to their individual single-component materials, due to their morphology and their junction structure at the interface. Sun *et al.* [25] synthesized dumbbell-like Au–$Fe_3O_4$ nanohybrids via thermal decomposition of $Fe(CO)_5$ on {111}-surfaced Au particles and subsequent oxidation in 1-octadecene solvent. TEM/HRTEM images of these Au–$Fe_3O_4$ core–shell and dumbbell-shaped nanohybrids are shown in Fig. 9.3. The sizes (~2–8 nm) of Au particles was controlled either by tailoring the molar ratio of $HAuCl_4$ to oleylamine or by controlling the temperature at which the $HAuCl_4$ solution was injected. The

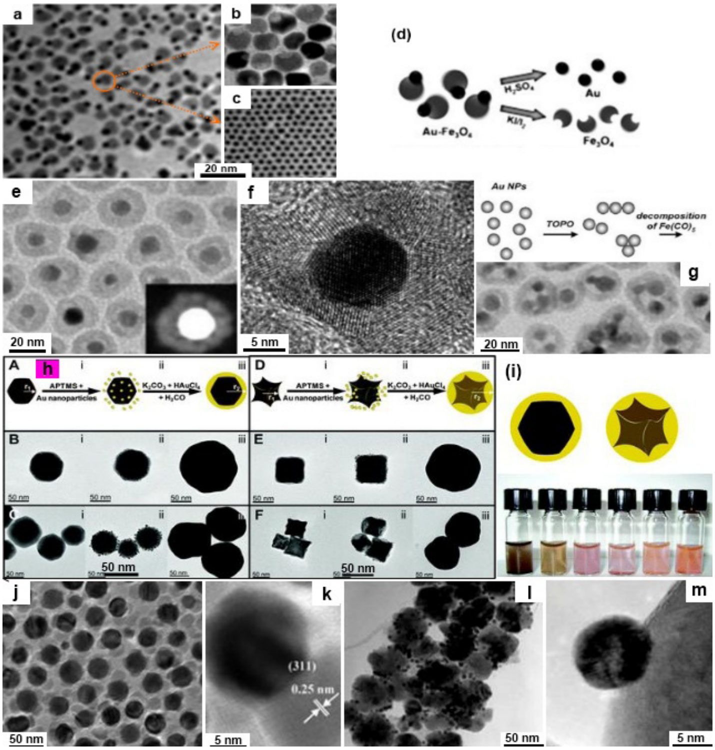

**Figure 9.3** Gallery of representative TEM/HRTEM images illustrating examples of dumbbell and core@shell nanohybrids made of metal and semiconductor associations. Etching of (a) Au–$Fe_3O_4$ nanohybrids for the preparation of (b) Au particles and (c) dented $Fe_3O_4$ particles, (d) illustrated scheme of the etching process [27]; (e, f) Hollow gold–iron-oxide core–shell nanohybrids, (g) formed hollow nanohybrids with multiple gold cores and corresponding scheme demonstrating the possible synthesis mechanism [28]; (h, i) Magnetic-plasmonic core–shell nanohybrids of Au coated iron oxide with various shapes [29]; (j, k) Au–$Fe_3O_4$ nanohybrids synthesized by thermal decomposition of mixtures of transition metal-oleate complexes and metal-oleylamine complexes [30]; (l, m) Au–$Fe_3O_4$ nanohybrids formed from the functionalized cysteine-linked $Fe_3O_4$ nanocrystals and Au [31].

sizes (~4–20 nm) of the $Fe_3O_4$ particles were tuned by adjusting $Fe(CO)_5$/Au ratio. TEM/HRTEM results revealed that the dumbbell-shaped structure was yielded by growing the {111}-faceted $Fe_3O_4$

onto the {111}-faceted Au. The oxidation of metallic Fe particles to $Fe_3O_4$ particles can be achieved, giving Au–$Fe_3O_4$ nanoparticles upon exposure to air [26]. The oleylamine/oleic-acid-capped Au–$Fe_3O_4$ nanodumbbells were synthesized and further functionalized by a surfactant exchange reaction. The polyethylene glycol (PEG)- and HS-PEG-$NH_2$-conjugated Au–$Fe_3O_4$ nanodumbbells were made to be biocompatible for medical applications. The Au–$Fe_3O_4$ nanodumbbells before and after surface modification exhibited room-temperature superparamagnetic character. The 8–20 nm-Au–$Fe_3O_4$ nanodumbbells showed a plasmonic absorption in phosphate buffered saline at 530 nm that shifted to the slight red as compared to 8 nm Au nanoparticles (at 525 nm), due to the junction effect on the dumbbell structure. The dumbbell structure of Au–$Fe_3O_4$ nanocrystals with the particle size ranging from 3–17 to 8–20 nm were also synthesized by controlled nucleation of $Fe_3O_4$ on Au particles [27].

Single-component Au and $Fe_3O_4$ nanoparticles were formed from Au–$Fe_3O_4$ nanohybrids by etching of Au–$Fe_3O_4$ species by etching $Fe_3O_4$ away from the Au–$Fe_3O_4$ nanohybrids on carbon catalyst in diluted $H_2SO_4$ solution and by a two-phase etching of Au from Au–$Fe_3O_4$ nanohybrids using KI/$I_2$ solution, respectively, as shown in Fig. 9.3a–d. The $H_2O_2$ reduction was studied using these single-component and Au–$Fe_3O_4$ hybride samples as catalysts. It is found that the enhanced activity of Au–$Fe_3O_4$ arose from the interaction of the Au–$Fe_3O_4$ interface, where the $Fe_3O_4$ nanoparticle surface became more active.

Using oleylamine as a mild reducing and capping agent at low temperature, the Au–$Fe_3O_4$ dumbbell nanohybrids were produced by depositing Au on the $Fe_3O_4$ nanoparticles in a chloroform solution [32]. After the synthesis, the Au–$Fe_3O_4$ nanohybrids were transferred from the organic environment to water with CTAB and sodium citrate. The water-soluble nanohybrids were served as seeds for the formation of Au–$Fe_3O_4$ nanoparticles with thicker Au coatings by adding more $HAuCl_4$ under reductive conditions. Further, using Au–$Fe_3O_4$ as seeds, Ag/Au–$Fe_3O_4$ nanodumbbells were also obtained by adding $AgNO_3$ to the reaction solution under the same synthetic condition. Figure 9.3e–g shows that the hollow Au–$Fe_3O_4$ core-shell nanohybrids were synthesized from the deposition of an iron shell around the gold core and then oxidized the metallic iron shell to form a hollow iron oxide shell on the basis of Kirkendall mechanism [28].

The capping oleylamine and oleic acid ligands at the surface of the preformed gold seeds could affect the ability of iron to deposit on the seed's surface.

The deposition of iron precursors onto gold particles depends on the different oleylamine/oleic acid molar ratios (Fig. 9.3e,f,g). At 1:1 oleylamine:oleic acid molar ratio, the thinnest oxide shell (~2 nm) around the gold nanoparticles was formed. The irregular iron-oxide shells with polycrystalline and connecting some places with the gold core were produced in the presence of oleylamine without oleic acid. The introduction of oleic acid into the synthetic solution led to a particle-size decrease of hollow iron-oxide nanoparticles and no nucleation and growth of iron occurred at oleylamine:oleic acid molar ratio of 1:2. The iron nucleation and growth were to be slowed in the increase of the oleic acid concentration due to the formation of stable iron-oleate complex in the high-temperature reaction solution. Similarly, Pt–$Fe_3O_4$ dumbbells could be produced by controlling the growth of Fe on Pt particles and followed by oxidation in air. The plasmonic-magnetic Au–$Fe_3O_4$ core–shell nanohybrids were also obtained by the growth of the gold shell layer around faceted and tetracubic-shaped magnetic iron oxide cores [29]. The growth of the Au shell layer on the $Fe_3O_4$ nanocrystals was expressed in Fig. 9.3h,i. The synthetic procedure illustrated that the surface of iron-oxide nanocrystals was functionalized with the amine-terminated linker molecule that allowed small Au nanodots to attach and grow further onto the nanocrystal surface for the formation of Au–$Fe_3O_4$ core-shells. Hyeon *et al.* [30] reported a general route to synthesize numerous metal@oxide heterostructures with diverse shapes via the thermal decomposition of mixtures of transition metal (Fe, Mn)-oleate complexes and metal (Au, Ag, Pt, Ni)-oleylamine complexes in organic solvent in the presence of oleylamine surfactant (Fig. 9.3j,k). Water-dispersed oligonucleotide-conjugated Au–$Fe_3O_4$ nanohybrids as a representative sample were prepared and used in multimodal biomedical probes.

Li *et al.* [31] expressed that the cysteine-linked $Fe_3O_4$ nanoparticles were carried out by the formation of amide bonds between the surface amino groups of the pre-synthesized $Fe_3O_4$ nanoparticles and the carboxylic groups of cysteine biomolecules. The $Fe_3O_4$ nanoparticles were then functionalized by thiol groups of alkylthiol ligand. The Au particles were prepared in aqueous media through the reduction of $HAuCl_4$ by $NaBH_4$. The bifunctional Au–$Fe_3O_4$ nanohybrids were prepared from the conjugation of

Au particles to thiol-modified $Fe_3O_4$ nanoparticles by the strong interaction between Au and thiol group under ultrasonic conditions. These results are shown in Fig. 9.3l,m. These materials showed not only excellent magnetic properties and highly efficient separation of the targeted protein, but also enhanced catalytic activity. The biomolecule lysine-assisted route could be expanded to fabricate the diverse noble-metal (Au, Pt, Ag, Pt/Au)/$Fe_2O_3$ hybrid nanoparticles [33]. Lysine contains both amino and carboxylic groups that play dual roles as both linker and capping agents in attaching metals onto $Fe_2O_3$ nanosupports. The hybrid sensors witnessed the significantly improved sensor performances in terms of high sensitivity and good reproducibility in comparison with pristine $Fe_2O_3$. Furthermore, bimetallic alloys were also considered an active site to deposit on the nanosupports of the enhanced reactive activity. For example, bimagnetic $Fe_{58}Pt_{42}$–$Fe_3O_4$ coreshells were synthesized from high-temperature-solution phase coating of 4 nm $Fe_{58}Pt_{42}$ core with 0.5–3 nm $Fe_3O_4$ shell. Magnetic-shell-thickness-dependent properties of the as-synthesized core/shell particles were found, due to the exchange coupling between core and shell. The self-assembled core/shell nanostructures were transformed into a hard magnetic nanocomposite with enhanced energy product upon reductive annealing [34]. The synthesis of active and durable catalysts for the oxygen–reduction reaction was one of the urgent needs in the development of fuel-cell devices for practical applications. Hybrid Pd/FePt NPs core/shell nanostructures with 5 nm Pd core and 1–3 nm FePt shell were synthesized by the decoration of FePt precursor on Pd seeds [35]. The FePt composition was controlled by the molar ratio of $Fe(CO)_5$ and $Pt(acac)_2$, and the FePt shell thickness was tuned by controlling the weight ratio of the Fe and Pt precursors and the Pd seeds. The uniform FePt coating on the Pd seeds was controlled by turning the $Fe(CO)_5$ amount. Pt did not nucleate on the Pd seeds in the absence of $Fe(CO)_5$. $Pt(acac)_2$/Pd seeds with weight ratios in the 3:1 to 2:1 range were critical for the formation of continuous FePt shells on the Pd particles. It was declared that oxygen-reduction-reaction catalysis of the Pd/FePt core–shell nanohybrids was dependent significantly on the FePt shell thickness. Such nanocatalysts having thin FePt shell (<1 nm) exhibited both active and durable for oxygen reduction reaction in $HClO_4$ solution. These Pd/FePt nanohybrids would be a promising new catalyst candidate for fuel-cell applications.

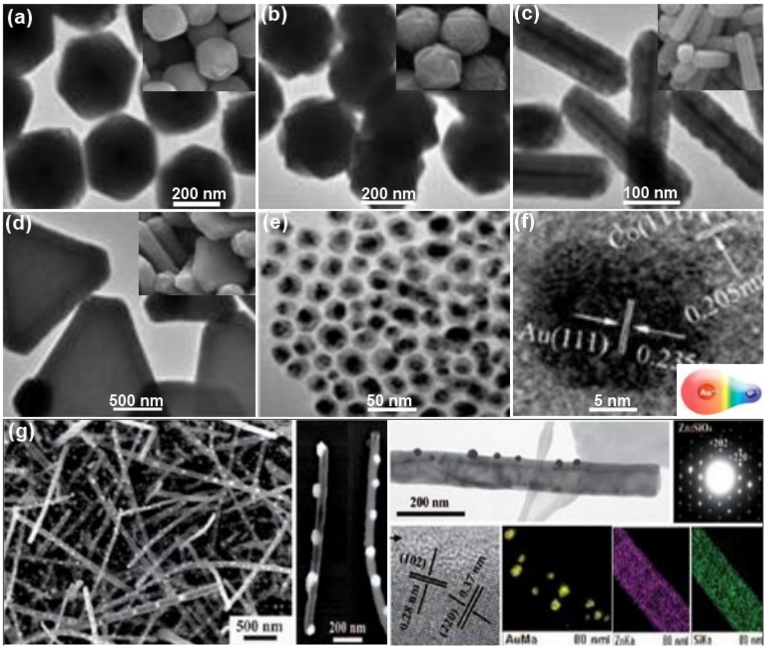

**Figure 9.4** Gallery of representative TEM/HRTEM/SEM images illustrating examples of dumbbell and core–shell nanohybrids made of metal and oxide associations: Au–$Cu_2O$ core–shell nanohybrids with (a) cuboctahedral, (b) truncated stellated icosahedra, (c) rod, (d) truncated triangular shapes [36]; (e, f) Au–Co core–shell nanohybrids [37]; (g) one-dimensional Au/$Zn_2SiO_4$ nanohybrids formed by annealing solid ZnO–Au–$SiO_2$ nanowires [38].

The nanocrystal-directed growth of Au–$Cu_2O$ core-shells with precise shape control and highly symmetrical shell morphologies using Au nanoplates, nanorods, octahedra as the structure-directing cores for the overgrowth of $Cu_2O$ shells was achieved by preparing a mixture of $CuCl_2$, sodium dodecyl sulfate surfactant, Au particles, NaOH, $NH_2OH{\cdot}HCl$ aqueous solution [36]. TEM/HRTEM results in Fig. 9.4a–d revealed that the Au particles were located at the center of the heterostructures. The six {100}-faceted cuboctahedral $Cu_2O$ shells were strongly attached on the octahedral Au core, indicating that the shell growth was guided by the shape of the Au core. The electronic properties of $Cu_2O$ might be modified by the inclusion of gold cores. Consequently, the electrical conductivity of the Au–$Cu_2O$ hybrid nanocubes showed the significantly better conductivity as compared to single $Cu_2O$ sample. The $Pd@CeO_2$ core–shell nanohybrids, as an active catalyst for CO oxidation, water-gas shift, and methanol steam reforming reaction, were synthesized by Fornasiero *et al.* [39] through adding the THF solution of MUA-Pd nanoparticles to the THF solution of cerium(IV)tetrakis(decyloxide), followed by the addition of a THF solution of dodecanoic acid. The hydrolysis of cerium(IV) alkoxide in the Pd–Ce solution was carried out by slowly adding $H_2O$ in THF for the formation of core-shells. Furthermore, Au-peapodded $Ga_2O_3$ nanowires were synthesized by thermal annealing of core–shell Au–$Ga_2O_3$ nanowires at a sufficiently high temperature. Au nanoparticles periodically encapsulated in the single-crystalline-monoclinic-phase $Ga_2O_3$ nanowires were based on the mechanism of Rayleigh instability [40]. In addition, the size and shape can be manipulated by changing the annealing time and/or the forming gas [41]. The combined deposited process and hydrothermal growth were used to produce the hybrid $SnO_2$ backbones/ZnO branches through epitaxial grown of the ZnO nanorods onto the side faces of the $SnO_2$ nanowires. The morphology of the ZnO backbones can be tailored by changing the precursor concentration, reaction time, and by adding surfactant. Such hybrid $SnO_2@ZnO$ nanostructures showed the enhancement of near-bandgap emission as compared to the pure $SnO_2$ nanowires possibly due to their complex 3D nanostructures with an ultrahigh surface area [42].

A variety of oxide materials has been enwrapped within a $SiO_2$ shell and were then used to transfer such nanomaterials to biological environments for specific cell targeting/sorting or MRI imaging purposes [43]. Gosele *et al*. [38] performed the atomic layer deposition of the 15 nm $SiO_2$ layer onto the Au–ZnO nanowires yielding the hybrid Au/$Zn_2SiO_4$ nanowires. From the SEM/TEM observations in Fig. 9.4g, the formed ZnO–Au–$SiO_2$ sandwich nanostructure was based on a controllable interfacial solid–solid reaction and Kirkendall effect. The 1D nanotubes were completely hollow or composed of discontinuous long tubular sections. The SAED pattern exhibited the diffraction spots, revealing the single crystals of the rhombohedral structure of $Zn_2SiO_4$. The outer surface of the $Zn_2SiO_4$ nanotubes was decorated with 50 nm-sized gold particles. It was also found that the thickness of the deposited gold interlayer strongly affected on the formation of perfect $Zn_2SiO_4$ nanotubes.

The Au-coated $TiO_2$ nanotube arrays were made up of the synthesis of a $TiO_2$ nanotube array with the wall thickness of 30 nm through a ZnO template and followed by deposition of 5 nm-sized Au particles onto the $TiO_2$ surface. The multifunctional properties, including SERS effect and photocatalytic degradation of persistent organic pollutant of Au-coated $TiO_2$ nanohybrids, were also reported [44]. The 5 nm Pt particles well-dispersed on the surface of $TiO_2$ nanowires were fabricated by a hydrothermal and chemical reduction process. Pt-$TiO_2$ hybrids could serve as effective catalysts because small-sized Pt incorporation on $TiO_2$ surface can accelerate the electron-hole separation and the charge transfer to dissolved oxygen molecules. The influence of Pt-loading values on photocatalytic efficiency was also found. The 1 wt% Pt–$TiO_2$ nanocatalysts exhibited the highest photocatalytic activity on methylene-blue degradation. However, a high Pt-loading value did not mean a high photocatalytic activity; higher content-loaded Pt nanoparticles could absorb more incident photons that did not contribute to the photocatalytic efficiency [45]. Hierarchical assembly of novel MnO@$WS_2$ hybrid nanotubes was yielded on the basis of the Pearson hardness (hard/soft acid-base). The route can be extended to the related carbon nanotubes and various oxide nanotubes for the attachment of electronically active components such as noble metal or semiconductors nanoparticles [46]. Pt@$AuNi_{0.5}Fe$ core–shell nanohybrids with high activity and stability for the oxygen–reduction reaction were synthesized by *in situ* decomposition of $AuNi_{0.5}Fe(CN)_6$ precursors in the presence of Pt seeds [47].

The Au@Ag core–shell nanocubes were also synthesized in high yield (86–90%) though seed-mediated growth [48]. (i) A two-step procedure was used to prepare the Au-nanocrystal seeds, in which 3 nm Au particles were generated by adding ice-cooled $NaBH_4$ solution into the aqueous solution containing $HAuCl_4$ and CTAB. CTAC-capped Au seeds were then formed from the reaction solution containing $HAuCl_4$, CTAC, ascorbic acid, 3 nm Au particles. (ii) The aqueous $AgNO_3$ solution was added to CTAC-capped Au seeds in the presence of ascorbic acid and CTAC for the fabrication of core–shell nanostructures. The edge lengths of the hybrid nanocubes could be finely controlled from 13.4 to 50.0 nm by using spherical-shaped Au seeds (11 nm) and cetyltrimethylammonium chloride surfactant to direct the overgrowth of Ag shells. Due to the spherical shape and high uniformity for the Au seeds, the thickness of the Ag shells could be precisely controlled from 1.2 to 20 nm. It is interestingly noted that the Au@Ag core–shell nanocubes were transformed into interior hollow nanocubes via a galvanic replacement process. The Ag shells were converted into porous Ag shells, while the Au cores were kept inside the shells. These size- and shape-controlled Au@Ag nanocubes also exhibit their unique optical properties.

The $Au_{core}$–$Co_{shell}$ nanohybrids were generated by thermal decomposition of $Co_2(CO)_8$ in toluene containing Au seeds and $HAuCl_4$ precursors [49]. During the synthesis reaction, atoms within the core–shell nanoparticles migrated to transform their initial core–shell morphology to a stable “peanut” structure. The morphological transformation was occurred by a well-defined series of energy minimization steps. Furthermore, a one-pot wet-chemical route to the Au-based hybrid magnetic nanostructures, including Au–Co core–shell nanocrystals with a core diameter of ~10 nm and a shell thickness of ~5 nm and Au–Ni spindly nanostructures with ~10 nm of tip size and ~15 nm of tail diameter, has been developed by Li *et al.* [37]. Accordingly, these hybrid nanocrystals were yielded by the solvothermal reaction of $HAuCl_4$ and transition metal nitrate ($Co(NO_3)_2{\cdot}6H_2O$ or $Ni(NO_3)_2{\cdot}6H_2O$) were used as starting materials and octadecylamine as surfactant and solvent. As seen in Fig. 9.4e,f, for the Au–Co core–shell nanohybrids, the measured lattice spacings of 0.235 nm for the core and 0.205 nm for the shell correspond to cubic Au{111} and cubic Co{111} facets. The lattice fringes with interplanar distances of 0.203 nm were found in both the tip and tail of the Au–Ni spindly structures. The high-angle annular dark-field scanning TEM images of both the products clearly showed the brighter contrast in the images, suggesting the formation of hybrid nanostructures. The Au–Co core–shell nanocatalysts exhibited the high catalytic activity toward CO oxidation as compared to that of pure Au and Co species. This could be due to the interfacial interaction between gold and transition metal particles and quantum size effect.

### 9.3.2 Metal@Semiconductor

The hybrid metal-semiconductor nanocrystals have attracted a great deal of attention due to their optic and photocatalytic applications [5]. Figure 9.5 shows representative TEM/SEM/HRTEM images of some examples of such metal-semiconductor hybrid nanomaterials that have been synthesized by direct heterogeneous nucleation and growth of the metal precursors onto preformed seeds. The difference in reactivity between the facets at the tips and at the sides of the CdS or CdSe nanoparticles has been documented. It was suggested that the anisotropic reactivity of the {001} tips of seeded CdSe/CdS nanorods resulted in the growth of metallic Au particles on only tips of the rod (Fig. 9.5a,b,c) [50]. The facets at the fast-growing end, which is further from the CdSe core, tend to be sulfur-rich, while the facets at the end closer to the CdSe core tend to be cadmium-rich. The strong Au-S interaction indicated that Au deposition first occurred primarily on the facets at the end further from the CdSe core, followed by the deposition on the facets at the end closer to the CdSe core. Under UV excitation, large Au domains may be exclusively deposited at one end of the seeded CdSe/CdS rod because of electron migration to one of the metal tips, whereas under ambient light conditions, the deposition of Au along the nanorod was strongly influenced by temperature-dependent, ligand-mediated defect sites. Precise control over the deposition of Au at specific locations on the anisotropic CdS core–shell nanorods not only would be critical for directed assembly but also should have the dramatic influence on the optical properties of the rods. Multicomponent nanostructures composing of 0D spheres and 1D nanorods had been produced by Banin *et al.* [51]. Further, the author also reported selective growth of gold onto the tips of CdSe rods and tetrapods [50]. The fluorescent quenching phenomenon that is characteristic of the Au–CdSe nanohybrids was observed owing to the strong coupling between the metal and the semiconductor.

Dumbbell-shaped nanostructures from each PbSe sphere and CdSe rod were also synthesized by Manna *et al.* [52]. Significant modification of optical spectra was observed for the dumbbell-shaped nanostructures compared to those of either the initial CdSe nanorods or PbSe nanospheres. Moreover, Klinke *et al.* [53] synthesized Au–CdSe rod- and pyramid-shaped nanohybrids via the growth and reductive transformation of a gold shell around pyramidal CdSe nanocrystals in the presence of chlorine under either electron beam irradiation or addition of a strong reducing agent during synthesis. The size of deposited gold nanodots can be tuned from 1.4 to 3.9 nm by varying the synthesis conditions, including the ligands or the shape of the CdSe nanocrystals. The shape rod and pyramid were thermodynamically favored for the size-controlled growth of Au precursors on the corners/edges and tips of the CdSe nanocrystals through the suitable choice of metal precursor and surface ligand concentration (Fig. 9.5d,e). The pyramid structure provided relatively sharp angles that were highly reactive sites for the nucleation of gold particles. The effect of the degree of mismatch between the crystal lattices of the two components has also been studied by Shim *et al.* [54] who examined the growth of different metal sulfides onto spherical $Fe_2O_3$ nanocrystals. Within these systems, the lattice mismatch of the semiconductors and iron oxide was 4.0% for ZnS, 4.6% for CdS, and 5.1% for HgS. As the amount of lattice mismatch increased, the authors observed fewer instances of junction formation between the semiconductor and magnet domains and an increasing occurrence of homogeneous nucleation of the semiconductor nanocrystals.

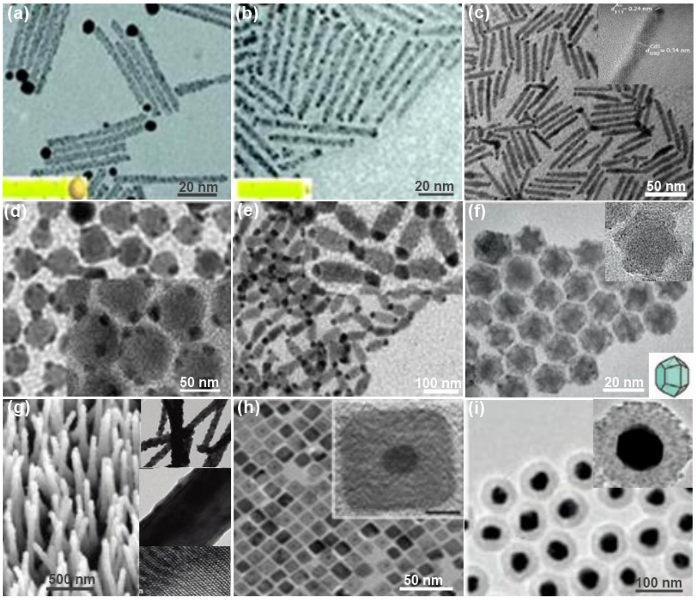

**Figure 9.5** Gallery of representative TEM/HRTEM/SEM images illustrating examples of dumbbell and core@shell nanohybrids made of metal and oxide associations. Au growth on CdS nanorods for 1 h: (a) dark at 313 K, (b) 473 nm laser irradiation at 313 K, (c) dark at 273 K [50]; CdSe-seeded CdS nanorods with varying degrees of Au deposition at (d) one end and (e) both ends of nanorod [53]; (f) Ru–$Cu_2S$ hybrid nanocages [55]; (g) ZnO–CdSSe nanorod grown on the Ti substrate [56]; (h) hybrid FePt–PbS nanocubes [57]; (i) hybrid Au–$SiO_2$–CdSe quantum dots particle [58].

Chan *et al.* [59] had used the ambient-light condition similar to the Banin's group to achieve the well-controlled deposition of Au on seeded CdSe/CdS nanohybrids by varying the additional Au precursor concentration [51]. The reactivity difference of the facets at the tips and sides of the nanorods caused the change of Au-decorated morphologies by adjusting the Au precursors concentration. Figure 9.5d,e shows TEM/HRTEM images of the resultant CdSe-seeded CdS nanohybrids with Au deposited at distinct locations on their surface. The trend of selective Au growth at one tip, both tips, and throughout the nanorod with increasing concentrations of additional Au precursor was found.

Very recently, the Banin's group had fabricated the cage-shaped Ru@$Cu_2S$ nanohybrids via adding the $Ru(acac)_3$ solution to a suspension of the pre-synthesized $Cu_2S$ nanoparticles in octadecylamine at 210°C [55]. As seen in the TEM image in Fig. 9.5f, the resultant Ru@$Cu_2S$ nanohybrids exhibited curious patterns of dark and light regions. HRTEM results revealed that the core of the nanohybrids was single crystalline and the protruding features suggested a frame structure around the core that was reminiscent of those seen of Au nanocages. The unique cage formation could be due to capping thiol-passivating ligands on the well-defined facets of the $Cu_2S$ particles leading to blocking growth of these facets. The Ru/$Cu_2S$ nanocages were an efficient electro-catalyst toward $H_2O_2$ sensing that was two orders of magnitude higher than that of the bare $Cu_2S$. The high redox catalytic activity could be due to the synergy of the two powerful concepts of unique cage shape and material combination. Yu *et al.* [60] reported that hollow Au–$PbS_x$ heterodimer nanoballs with a diameter around 9.3 nm and the wall thickness in the range of 2–4 nm were built from hollow $PbS_x$ and solid Au domains have been synthesized by a mild reaction between the gold species and PbS nanocrystals in dodecylamine. Liu *et al.* [61] reported the synthesis and optical properties of $Ag_2S$- and $Ag_2Se$-coated Au nanohybrids. Sodium sulfide or selenourea was then reacted with the silver coating, resulting in the conversion of the silver layer into the $Ag_2S$ or $Ag_2Se$ shell. The seed shape and shell thickness could be tuned independently, resulting in nanohybrids with tunable optical properties.

The hybrid materials composing of multicomponents have also been fabricated and designed recently. Pang *et al.* [62] developed a general synthesis of core–shell structured noble metal (alloy) cadmium-selenide nanocrystals, including FePt/CdSe, NiPt/CdSe, FePt/CdSe, NiPt/CdSe via the hydrolysis of cadmium stearate in oleylamine, hexadecylamine, or octyl ether, 1,2-hexadecandiol in the presence of alloy seeds. The clear crystal structured nanohybrids were indicative of the 4 nm core and 2–3 nm shell. Using the same synthetic procedure, Au–CdSe core–shell nanohybrids were fabricated by coating Au core with a CdSe shell in oleylamine. Au–PbS core–shell nanostructures were also produced by injecting the pre-prepared Pb-oleate complex into dodecanethiol-capped Au nanocrystals in toluene [63]. The growth of PbS shells on Au seeds was initiated by the injection of bis(trimethylsilyl)sulfide dissolved in 1-octadecene under vigorous stirring at 130°C for 5–10 min. The Au–PbS core–shell materials displayed the enhancement of the absorption spectra due to the synergistic coupling between plasmon and exciton in the core and shell. Moreover, the Au–PbS core–shell nanostructures demonstrated strong *p*-type doping materials due to the formation of an intra-particle charge transfer complex. While Park *et al.* [56] had fabricated vertically aligned ZnO–CdSSe core–shell nanoarrays with a controlled composition and shell thickness via the chemical vapor deposition on the pre-synthesized ZnO nanowire arrays (Fig. 9.5g). The experimental results revealed that the deposited ZnO shell with single crystallinity grew along the [0001] wire axis of the wurtzite ZnO core. The (002) fringes were separated by a constant distance that was close to that of the bulk. This approach was also applied to fabricate the high-quality $TiO_2$–CdS and ZnO–$CdS_{0.5}Se_{0.5}$ core-shells. The successful development of such ZnO- or $TiO_2$-based photoelectrochemical cells would be a key step toward the construction of the novel viable nanometer-scale solar cell devices. The electronic structures of the CdSe/CdS core–shell nanorods were systemically investigated by Wang *et al.* [64]. The effects of band alignment, quantum confinement, piezoelectric field, dipole moments were analyzed and delineated by comparing the results of systems with or without some of these attributes. The authors found complicated interplays between these effects in determining the nanorod bandgap and electron-hole wave function localizations. The hole wave function was found to be localized inside the CdSe core, while the electron wave function was localized in the CdS shell, with its distance to the CdSe core depending on the surface passivation. The permanent dipole moment induced by different surface passivations could change the electron-hole separation, while the piezoelectric effect played a relatively minor role. This route was also straightforward to manipulate the nanorod electronic structure by changing its CdSe core position.

Colloidal FePt@PbS and FePt@PbSe heterogeneous nanostructures with effective optical, magnetic, electrical, magnetotransport properties were synthesized by combining a ferromagnetic FePt nanocrystals with either the quantum-confined PbS or PbSe semiconductors in form of core-shells or nanodumbbells through seed-mediated growth (Fig. 9.5h) [57]. The products were formed by the injection of bis(trimethylsilyl) sulfide into the reaction mixture containing monodisperse FePt nanocrystals, oleic acid, Pb-oleate complex dissolved in 1-octadecene at 120–150°C for 5–10 min. The shape of products was controlled by the reaction temperature and the capping ligands on the surface of FePt seeds. $CuInSe_2$/$CuInS_2$ core/shell nanocable bundles were recently synthesized by adding sulfur to the reaction system, and the shell thickness of the polycrystalline $CuInS_2$ in the nanocables increased with increasing S/Se molar ratios. The $CuInS_2$ shells were formed possibly due to the small radius of copper ion that can allow their fast outward diffusion from the interior surface of nanowires to react with sulfur elements and indium ions [65]. Hybrid PbSe/CdSe/CdS nanocrystals with two distinct geometries: core/shell/shells and tetrapods were synthesized and demonstrated the efficient emission in the IR with exceptionally long exciton lifetimes. These materials would be attracted for a variety of applications from lasing to photocatalysis and photovoltaics [66]. Well-defined hybrid Au/$SiO_2$/CdSe nanostructures comprising a gold core overcoated with a silica shell, following by a dense monolayer of colloidal CdSe quantum dots were formed through a multistep procedure (Fig. 9.5i). The formed products involved the synthesis of gold nanoparticles, gold-particle surface activation, silica-shell deposition, modification of the silica surfaces with $-NH_2$ groups, and final self-assembly of CdSe quantum dots onto the particle surface [58]. For the surface activation of the Au particles, (3-mercaptopropyl)-trimethoxysilane was used, because of its strong binding of the –SH groups to the gold surface. These hybrid structures were used to perform the accurate quantitative analysis of the effect of the metal on quantum dot photoluminescence intensity.

### 9.3.3 Bimetallic Metal@Metal

Bimetallic nanocrystals provide a new system with tunable catalytic and optical properties sought for applications in catalysis, diagnosis, plasmonics, and surface-enhanced Raman spectroscopy, etc. [67]. The physiochemical properties of bimetallic nanohybrids can be tailored by controlling their size, shape, elemental composition, as well as the internal and surface structures. Recently, the complexity of nanomaterials can be enhanced further by the formation of multimetallic nanostructures. These heterogeneous core–shell nanostructures can often be achieved via the deposition of a metal on the core surface of another metal or a galvanic replacement reaction between the core and a salt precursor as a second metal.

For example, the tips and the side surface of Au nanorods had been coated with other metals such as Pd, Pt, Ag, and Ni to create new functions to the Au nanorods [68–72]. The development of these structures is motivated that they provide a new system with tunable novel collective properties. Figure 9.6 displays a gallery of representative TEM and HRTEM images of bimetallic nanohybrids. Xia *et al.* [73] reported on the synthesis of the uniform Au@Ag core–shell materials with a uniform size distribution were composed of Ag nanocrystals containing Au nanorods in the center (Fig. 9.6a,b). The dimensions of the core–shell nanostructures were easily tuned by using Au nanorods with different aspect ratios and/or by controlling the amount of $AgNO_3$ added into the reaction system. With an increase in the $AgNO_3$ amount, the Ag started to grow faster on the side surface of the Au nanorod and the shape evolved into an octahedron. PVP and CTAB ligands affected both the deposition of Ag and the final shape of the core–shell nanostructure. The Au@Ag core–shell nanostructures showed one broad peak at ~460 nm and a shoulder peak at ~350 nm. The formation of Ag shell on Au nanorod in hexadecyltrimethylammonium chloride (CTAC) and hexadecyltrimethylammonium bromide (CTAB) mixed micellar solutions were also achieved [74]. It is found that the Ag shell formation in a CTAC solution was much faster than that in a CTAB solution. The uniform Au–Ag core–shell nanorods were obtained by retarding the silver shell growth on gold nanorods. The colloidal solutions of the Au–Ag core–shell nanorods showed the four extinction bands that originated from the anisotropic silver shell formation. The thickness of the anisotropic silver shells could be controlled by the relative amounts of silver ions and gold nanorods. The extinction spectra, photographs of the dramatic changes in color from orange to green of the reaction solution, and TEM images of the elongated shape of the anisotropic Au–Ag core–shell nanocrystals using $AgNO_3$ solutions at the different Ag/Au molar ratios are shown in Fig. 9.6d [75]. Ag@Au core–shell nanocrystals were prepared by coating Au nanodumbbells with silver in an aqueous solution containing CTAB, $AgNO_3$, NaOH, ascorbic acid. The morphology observation showed that Ag grew on top of the Au dumbbell core, rather than growing on the side of Au. The Au@ Ag core-shells served as excellent SERS substrates, as significantly higher enhancement factors were expected for silver as compared to gold [76]. Photochemical route to the CTAC and sodium-dodecyl-sulfate-assisted synthesis of Au–Ag alloys and core-shells was also reported by Scaiano *et al.* [77]. Ag@Au core–shell triangular bifrustum nanocrystals were synthesized in aqueous solution using a seed-mediated approach. The formation of the Ag layer on the Au nanoprism seeds led to structures with highly tunable dipole and quadrupole surface plasmon resonances [78]. Very recently, Xia group used the seed-mediated growth process to synthesize the well-defined Au@Ag core–shell nanocubes [48]. The synthetic procedure of the Au seeds consists of two steps: (i) 2–3 nm Au nanoparticles were prepared by reducing $HAuCl_4$ with $NaBH_4$ in the presence of CTAB, and (ii) these Au particles grew into 11 nm Au nanocrystal seeds with cubo-octahedral shape in $HAuCl_4$/ascorbic acid/CTAC. The Au@Ag core–shell nanocubes were formed by depositing Ag on the as-prepared CTAC-capped Au seeds via adding $AgNO_3$, ascorbic acid, CTAC into an aqueous suspension containing the Au seeds at 60°C. The Ag shell thickness could be finely tuned from 1.2 to 20 nm by varying the $AgNO_3$/Au molar ratio. The LSPR properties of the Au@Ag core–shell nanocubes were found as a function of the Ag shell thickness. The edge length of the cubes increased from 24.4 to 50.4 nm when the concentration of the Au seeds was reduced from 14.6 to 1.46 mg/L. When CTAC was displaced by CTAB as capping agent, the resultant core–shell nanocrystals with controlled cube shape formed with difficulty, possible due to the primary formation of AgBr precipitates. The Ag shells of the hybrid nanocubes could be transformed into porous Au shells with slightly enlarged dimensions while the Au cores were kept inside the shells via a galvanic replacement process because the reduction potential of Ag is the lower than that of Au.

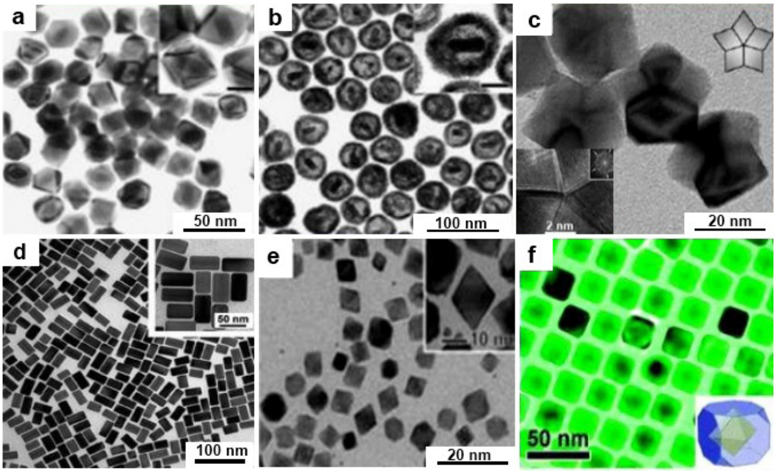

**Figure 9.6** Gallery of representative TEM/HRTEM images illustrating examples of bimetallic nanohybrids: (a) Au@Ag core–shell nanostructures with a mean diagonal length of 64.8 nm [73]; (b) Pt-based hollow nanostructures containing Au nanorods in the center [73]; (c) alloy Pd–Pt star-shaped decahedrons [79]; (d) anisotropic Au–Ag core–shell nanorods [75]; (e) Pd–Pt core–shell octahedrons [80]; (f) Au@Pd core–shell nanocubes [81].

For bimetallic Au and Pd system, it would be interesting to use Au nanocubes as the structure-directing cores for the overgrowth of Pd shells. Because of a significant lattice mismatch between gold and palladium, the resultant Au–Pd core–shell nanocrystals may exhibit unusual morphologies and high-index facets. Such nanocrystals with high catalytic activities may be obtained. The Pd–Au core–shell nanocubes and spherical nanostructures were formed by reducing $HAuCl_4$ with L-ascorbic acid in the presence of cubic Pd seeds in an aqueous solution. The dark-field scanning TEM result showed a clear contrast between the Pd core and the Au shell, confirming the core–shell structure. The Pd cores retained their original cubic shape, indicating that they were intact during the deposition of the Au shells. The synthesized Pd–Au bimetallic nanocrystals that combine the properties of both Pd and Au can generate the novel catalytic properties and potential applications, including *in situ* monitoring of catalytic reactions via surface-enhanced Raman scattering [82]. Two-step seed-mediated growth method for synthesizing single-crystalline 41.5 nm-sized Au@

Pd nanocubes was performed in high yield via the overgrowth on the octahedral Au cores with 30 nm in diameter by reducing $H_2PdCl_4$ with ascorbic acid under the assistance of CTAB surfactant (Fig. 9.5f). The different deposition of metal shell on the core for the overgrowth core–shell process was revealed by Ostwald ripening mechanism. Synthetic parameters such as a reducing, capping agent, metal ion, and reaction temperature could also play an important role in the overgrowth process [81]. Very recently, Huang *et al.* [83] synthesized the Au–Pd core–shell heterostructures possessing an unusual tetrahexahedral morphology with {730} facets in high yield via an aqueous-based method. Tetrahexahedral Au–Pd core–shell nanocrystals with eight progressively increasing dimensions from 56 to 124 nm were conveniently yielded as using different-sized cubic cores and adjusting the volume of the gold core solution added. In addition, by decreasing the reaction temperature and increasing the reaction time, novel concave octahedral and octahedral Au–Pd core–shell nanocrystals with both {111} and {100} facets exposed could be synthesized. The tetrahexahedral Au–Pd core–shell catalyst with entirely high-index {730} facets exhibit a higher electrocatalytic activity for the oxidation of ethanol than that of the other two Au–Pd heterostructures with low-index facets. Zhang *et al.* [84] developed a general single-step strategy for monodisperse AuPd and AuPt alloy nanocrystals with octahedron and rod shapes and an average size of 7 nm and tested the catalytic activity of the heterogeneous Suzuki coupling reactions on these catalysts.

The Xia's group synthesized the 40 nm-sized Pd–Pt-alloy star-shaped decahedrons and truncated triangular nanoplates with truncation at twin boundaries through the co-reduction of $Na_2PdCl_4$ and $K_2PtCl_4$ with poly(vinyl pyrrolidone) in aqueous solution [79]. High-resolution TEM/HRTEM images (Fig. 9.6c) of the star-shaped decahedron clearly revealed that it was composed of five single-crystalline domains with a twin-based adjoining plane between two neighboring domains. Multiplying twin defected structures can result the coalescence of both small single-particles. The crystal structure of the alloy nanocrystals could be controlled by manipulating the reduction kinetics by using different reducing agents such as PVP and EG. Alloy nanostructures made of Pd and Pt can be of particular interest owing to their wide applications in catalytic and electrocatalytic reactions. Recently, monodisperse and highly selective sub-10 nm Pd–Pt heterostructured ultrathin nanowires have also been synthesized through using Pd nanocubes as seeds in aqueous solution [85]. Pd-Pt bimetallic nanodendrites were consisted of a dense array of the Pt branches onto the core of 9 nm truncated octahedral Pd seeds by reducing $K_2PtCl_4$ by L-ascorbic acid in the aqueous solution. The Pt branches supported on faceted Pd nanocrystals exhibited relatively large surface areas and particularly active facets toward the oxygen reduction reaction. These Pd–Pt bimetallic nanodendrites can also find use as catalysts beyond fuel cell applications [86]. Yang and co-workers rationally designed and used cubic Pt nanocrystals as seeds for the conformal shape-controlled epitaxial overgrowth of Pd and the anisotropic growth of Au [87]. They also showed that lattice mismatch (0.77% for Pt/Pd versus 4.08% for Pt/Au) plays a critically important role in the overgrowth of the secondary metal and high lattice mismatch prevents the conformal overgrowth. Further control of Pt overgrowth on the surface of Pd nanocrystals with well-defined morphologies is expected to provide a promising route to the development of Pt-based catalysts or electrocatalysts with greatly improved activity and cost-effectiveness. Xia *et al.* [80] recently reported a systematic study on the epitaxial overgrowth of Pt on well-defined Pd nanocrystals with different shapes with exposed facets, including regular octahedrons, truncated octahedrons, and cubes (Fig. 9.6e). They clearly demonstrated that the mode of epitaxial growth of Pt on Pd nanocrystals can be controlled by employing a surface capping agent and manipulating the kinetics for Pt reduction. Pd@Pt core–shell nanostructures with controllable composition synthesized via the reduction of $K_2PtCl_4$ and $PdCl_2$ solutions with different molar ratios in the presence of CTAB upon microwave heating condition. The Pd@Pt electrocatalysts showed higher catalytic activity than pure Pd and pure Pt catalysts for the oxygen electro-reduction reaction and methanol electro-oxidation reaction, and the highest activity obtained at the Pd@Pt electrocatalyst with 1:3 molar ratio of Pd/Pt [77].

Au@Pt nanocolloids with nanostructured dendritic Pt shells were synthesized by reducing both $H_2PtCl_6$ and $HAuCl_4$ species in the aqueous solution containing low-concentration Pluronic F127 surfactant as a structural-directing agent. The Pt shell thicknesses on Au cores can be easily tuned by controlling the Pt/Au molar ratio. The Au@Pt core–shell nanocatalysts exhibited enhanced activity for the methanol oxidation reaction [88]. The bimetallic Au–Pt nanorods were grown *in situ* and embedded into thermosensitive core–shell microgel particles by a novel two-step approach. Firstly, 6.6 nm × 34.5 nm Au nanorods were homogeneously embedded into the shell of poly-*N*-isopropylacrylamide networks. Then platinum was preferentially deposited onto the tips of Au rod-shaped seeds embedded in microgel particles to form dumbbell-shaped Au–Pt nanocrystals that had the high catalytic performance for 4-nitrophenol reduction [89]. The synthesized Ru@Pt core–shell catalyst for preferential oxidation of carbon monoxide in hydrogen was studied by Eichhorn *et al.* [90]. Xia and co-workers [91] have introduced a general approach to produce hollow nanocages and nanocubes of metals by using the galvanic-replacement reaction principle. The products show similar visible-NIR tunability by control of the wall thickness and void size of the particle. This approach has been used to produce a variety of hollow/porous Au-, Pd-, and Pt-based nanoparticles from Ag nanoparticles. The hollow/solid $Ag_2S$/Ag heterodimers were synthesized at room temperature through the synthesis of monodisperse $Cu_2O$ solid spheres, conversion of the $Cu_2O$ to CuS hollow spheres, and ion-exchange of the resultant CuS to $Ag_2S$ hollow spheres. The Ag@$Ag_2S$ nanohybrids were formed via the photocatalytic reduction of the metallic silver phase on the resultant $Ag_2S$ heterodimer nanocrystals in the existence of the organic ligand ethylenediamine. Such highly asymmetric heterodimers exhibited strong bactericidal effects on *E. coli* K-12 upon UV-light irradiation [92].

## 9.4 Application of Nanohybrids as Nanocatalysts for CO Oxidation Reaction

The hybrid metal-oxide nanocrystals often exhibit an enhanced catalytic activity that raise from the particle–particle interaction. Therefore, different aspects have been studied in order to explain such extraordinary catalytic behavior, including the nature of noble-metal active sites, the influence of support, the preparation method, the preparation conditions, the metal particle size and oxidation state, and the catalyst pretreatment method. El-Shall *et al.* [93] reported a remarkable enhancement of the catalytic CO-oxidation activity at low temperature and directly correlated with the change in the morphology of the supported catalyst and the efficient dispersion of the small-sized active noble-metal (Au, Pd) particles on the oxide ($CeO_2$, CuO, ZnO) supports. Cao *et al.* [94] demonstrated that the surface structure or the morphology of ceria markedly affects the dispersion and reducibility of Au/$CeO_2$ catalysts. Most of the cited studies attribute the activity of ceria-supported Au to a direct interaction between the metal and the support. The extent of such interaction, related to the gold particle size and to the support morphology, would affect the electronic state of the $CeO_2$ substrate. On the other hand, Petrov *et al.* [95] suggested that the high activity of gold/ceria catalysts is due to the enhanced electron transfer between defective ceria and partially charged gold particles via oxygen vacancies, with formation of a complex between partially charged gold clusters and the support, so that the oxidation reaction proceeds at the interface between small gold clusters in an intimate contact with ceria. Catalytic activities of $CeO_2$ nanorods and gold nanoparticles on the $CeO_2$ nanorods as a function of reaction temperature are shown in Fig. 9.7a–e.

It is noted that the CO conversion increases with increasing reaction temperature for all samples. An 81% CO conversion was achieved at 220°C for Au/$CeO_2$ nanorods as catalyst, while only 20–22% CO conversion was obtained at the same temperature for pure $CeO_2$ nanorods and nanoparticles as catalyst. The catalytic activity of Au/$CeO_2$ nanorods and Au/$CeO_2$ nanoparticles was much higher than that of pure $CeO_2$ nanorods and nanoparticles. There could be a synergistic interaction between gold and $CeO_2$ nanoparticles [96]. Corma *et al.* [97] found the $CeO_2$ and rare-earth oxide nanocrystals can significantly increase the catalytic activity of dispersed Au nanoparticles for CO oxidation. The decoration of Au nanoparticles on the support of stable $CeO_2$ nanorods could efficiently prevent Au nanoparticles from the agglomeration. Recently, Venezia *et al.* [98] found that the reactive oxygen on the surface of nanocrystalline $CeO_2$ and the strong interaction between cationic gold and ceria might determine the high activity for CO conversion. The smaller $CeO_2$ nanoparticles might supply more active sites and contributed to the strong interaction between gold and nanocrystalline $CeO_2$. Therefore, the catalytic activity of Au/$CeO_2$ nanoparticles was better as compared to that of Au/$CeO_2$ nanorods. However, the thermal stability of the Au/$CeO_2$ catalyst was also an important factor for application. The $CeO_2$ nanorods, with the higher crystallinity and larger particle size, had a high thermal stability, which enhanced the durability of the catalyst. The 1 wt% Au@$CeO_2$ nanocatalysts prepared from embedding Au particles into $CeO_2$ nanosupports by surfaced carboxylic groups showed good activity under real preferential CO oxidation and better activity than corresponding catalysts with higher metal loadings (1–3 wt%). These catalysts were prepared via deposition precipitation with urea [99]. Reaction mechanisms for the CO oxidation on Au/$CeO_2$ catalysts were illustrated, in which the interplay between the reversible $Ce^{4+}$/$Ce^{3+}$ and $Au^{3+}$/$Au^{+}$ reductions underpins the high catalytic activity of dispersed Au atoms into the ceria substrate [100]. The high catalytic activity of the low Au-loaded $CeO_2$-nanoparticle catalysts can be attributed to their large surface area as well as the coexistence of $Au^{\delta+}$ ($Au^{+}$ and $Au^{3+}$) and $Au^{0}$ species, in which $Au^{+}$ acted as a dominantly active species. During the catalytic reactions, $Au^{3+}$ was probably reduced to $Au^{+}$, which enhanced the catalytic oxidation of CO [101].

Ambient-temperature CO oxidation activity of Pd/$CeO_2$ was found to increase by more than 20 times after thermal aging at 900°C in air (Fig. 9.7f). Although the aging resulted in a significant sintering accompanied by a 92% loss of surface area from 92 to 7 $m^2g^{-1}$, Pd metal dispersion was preserved at a high degree. Owing to the formation of Pd–O–Ce bonding at the PdO/$CeO_2$ interface, 1–2 nm-sized Pd oxide species were highly dispersed into the surface structure of $CeO_2$ that would provide active sites for CO adsorption and following reactions with oxygen near room temperature [102]. Boronin *et al.* [103] reported that ambient temperature activity to CO oxidation could be achieved by Pd highly dispersed on $CeO_2$, which consists of the surface interaction phase ($Pd_xCeO_{2-\delta}$) and very small Pd metal clusters (<1 nm).

Fornasiero *et al.* [39] used dispersible Pd@$CeO_2$ core–shell nanohybrids prepared by microemulsion as a flexible precursor to fabricate the active Pd@$CeO_2$/$Al_2O_3$ catalysts toward preferential CO oxidation. Hoang *et al.* [104] found that the Au/$Pr_6O_{11}$ nanorods exhibited a superior catalytic activity for CO oxidation, due to the synergistic interaction between Au nanoparticles and $Pr_6O_{11}$ nanorods and oxide migration from the support to the surface of the 8–12 nm Au nanoparticles. In addition, lattice oxygen atoms and isolated point defects of $Pr_6O_{11}$ usually play an important role in CO oxidation [104]. The catalytic activity of a variety of the selected bimetallic nanoalloys (5 wt%) supported on $CeO_2$ nanoparticles prepared by the microwave irradiation method was reported by Alghamdi *et al.* [105]. As shown in Fig. 9.7f,g,h,i, the highest activity was observed for the nanoalloys according to the order CuPd > CuRh > AuPd > AuRh > PtRh > PdRh > AuPt. Both the CuPd and CuRh supported nanoalloys showed promising results as efficient

CO oxidation catalysts with 50% conversions at 74 and 95°C, respectively. The highest conversions for these catalysts were 94% and 96% observed at 86°C and 158°C, respectively. The authors also declared that by alloying Pd into Au, the catalytic activity of Au for CO oxidation can be enhanced.

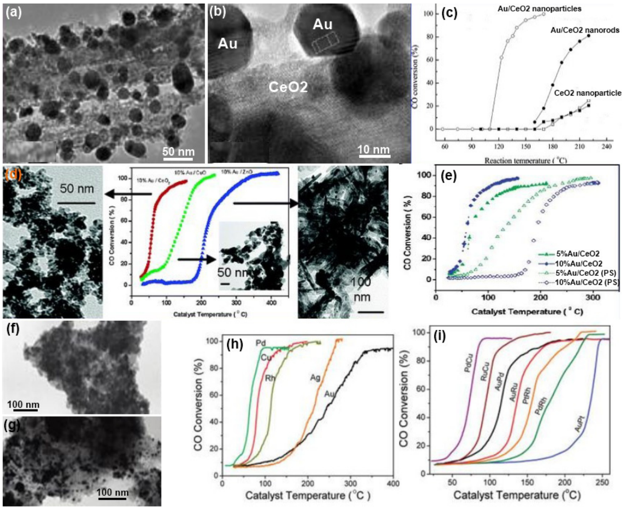

**Figure 9.7** CO oxidation catalytic activity over hybrid metal-oxide nanocrystals: (a, b) Au/$CeO_2$ nanorods, (c) Conversion of CO over Au/$CeO_2$ nanorods, Au/$CeO_2$ nanoparticles, $CeO_2$ nanoparticles [94]; (d) Conversion of CO over 10% Au/$CeO_2$ (red line), 10% Au/CuO (green line), 10% Au/ZnO (blue line) nanocatalysts, and (e) conversion of CO over Au/$CeO_2$ nanocatalysts with different Au components [93]; (f) Pd/$CeO_2$, (g) Cu/$CeO_2$, (h) CO oxidation on different metal/$CeO_2$ nanoparticles, (i) CO oxidation on different bimetallic nanoalloys supported on $CeO_2$ nanoparticles [105].

Catalysts based on combinations between copper and ceria constitute a more interesting alternative from an economical point of view. It is generally agreed that optimum catalytic properties for CO oxidation over copper–ceria catalysts are achieved in the presence of well-dispersed copper oxide patches over ceria nanoparticles [106]. Inverse $CeO_2$/CuO nanocatalysts were used as an alternative to classical direct configurations for preferential oxidation of CO in hydrogen-rich stream. The inverse $CeO_2$/CuO catalyst displayed the high CO oxidation activity as compared to the classical reference catalyst ($Cu_{0.2}Ce_{0.8}O_2$). The active sites for the CO oxidation reaction were related to interfacial $Cu^+$ species generated through a reductive process upon interaction with the CO oxidation reactant mixture [107]. The $Ce_{1-x}Eu_xO_{2-x/2}$ system presented a high number of surface oxygen vacancies, especially when the amount of dopant was around 10% (w/w). The resultant solid showed the enhanced catalytic properties for the CO oxidation reaction [108].

Haruta *et al.* [109] reported that $Au/TiO_2$ was a very good catalyst for CO oxidation under ambient conditions. The best performance was obtained for a catalyst calcined at 200°C and left at room temperature for a few days. The activity for CO oxidation was greatly influenced by moisture in the reactant gas, and a maximum was observed at around 200 ppm. Goodman *et al.* [110] found that Au nanoparticles of about 3.5 nm showed the highest activity in a series of $Au/TiO_2$ model catalysts. Although the active catalysts commonly contain small (2–5 nm) Au nanoparticles, the size of Au particles alone does not seem to be a sufficient factor for the high activity of nanosized Au catalysts. For instance, Vannice *et al.* [109] found that deposition of $TiO_x$ over-layers onto inactive Au powders (10 μm) can also produce very active $TiO_2$–Au catalyst for CO oxidation. In the attempt of Rolison *et al.* [111], the loading of ~6 nm Au nanoparicles onto $TiO_2$ sized to 10–12 nm produced composite $Au/TiO_2$ catalyst that exhibited high activity for CO oxidation, while Au particles of similar sizes were found inactive on commercial $TiO_2$ powders. It can be expected that such interaction at the metal-oxide boundaries can be properly tuned by systematically reducing the particle size of the support oxides. Bond *et al.* [112] reported inconsistent catalytic results of gold seeded on different titania supports (10 to 305 $m^2/g$) and observed that gold on anatase (37 $m^2/g$) showed the highest CO conversion rate. Ir and Au–Ir supported on $TiO_2$ catalysts exhibited the higher CO oxidation performance than that of $Au/TiO_2$ catalysts, due to their synergetic effect. The bimetallic catalyst was more stable in time on stream and more stable against sintering after reaction [113].

Yan *et al.* [114] achieved the deposition of 7 nm-sized Au nanoparticles on the mesoporous $CeO_2$–$Al_2O_3$ nanosupports prepared by the homogeneously dispersed 8 mol% ceria nanocatalyst with the size of 3–4 nm stabilized with ordered mesoporous alumina for the CO oxidation activity in comparison with pure mesoporous alumina and pure ceria nanoparticles. The evolution of the CO conversion as a function of temperature is presented in Fig. 9.8a,b. The sample 1 wt% Au/mesoporous $Al_2O_3$ gives 100% CO conversion at 150°C, while 1 wt% Au/$CeO_2$ gave a higher activity with 100% conversion at 120°C. The 8 wt% Au/mesoporous Ce–Al oxide catalysts exhibited excellent catalytic activity with 100% conversion occurring at 26°C, which was much better than the above two catalysts. This could be attributed to the strong synergistic interaction between the noble metal Au and $CeO_2$ and the nature of the mesosupport in determining the metallic Au catalysts' activity. This effect was related to the presence of a higher amount of oxygen vacancies in the ceria–alumina support. The coexistence of mixture of cationic and metallic gold in Au-supported catalyst generating the interaction effect of ceria catalyst and meporous alumina support could result in the high degree of CO adsorption and promoted the CO oxidation reactivity. Elam *et al.* [115] synthesized the bimetallic Ru–Pt particles doped on alumina sphere via atomic layer deposition (Fig. 9.8c). Methanol-decomposition reactions further confirm a Ru–Pt interaction and show enhanced methanol conversion for the bimetallic nanoparticles when compared to catalysts comprised of a mixture of pure Pt and Ru nanoparticles of similar loading (Fig. 9.8d). Gomez *et al.* [116] reported that the Au/In–$TiO_2$ catalysts were more stable than the Au/$TiO_2$ parent catalyst, the resulting Au/In–$TiO_2$ catalysts (6 and 12 wt % of In) were more active than the Au/$TiO_2$ parent catalyst for CO oxidation (Fig. 9.8e,f,g).

Influence of synthesis parameters, such as selection of support, reaction pH, aging time, and heat treatment, of the synthesis of Au-decorated silica–titania core-shell on the CO oxidation activity, as shown in Fig. 9.8h,i [117]. Namely, highly dispersed gold over the 600°C core-shell supports was obtained at pH 6.4–8.0 with an aging time of 30 min. The 3 nm active metallic gold could be obtained conveniently after mild heat treatment (<200°C), but from 300 to 400°C, agglomerates (6–20 nm) that are less active toward CO catalytic oxidation appear. The optimized material was synthesized at pH 6.4, displayed high loading and good dispersion of small-sized gold, and achieved 100% CO conversion at 35°C. Very recently, Mitarai *et al.* [122] reported that the $SiO_2$-supported 2.5 nm $Pt_3Ti$ nanocatalyst exhibited a higher catalytic activity toward CO oxidation than a $SiO_2$-supported Pt nanocatalyst containing a twofold more amount of Pt. $SiO_2$-supported $Pt_3Ti$ catalysts were not deactivated during catalytic oxidation of CO at elevated temperatures. $Pt_3Ti$

nanoparticles have promise as a catalytic center for the purification of automobile exhaust in terms of their high catalytic activity toward CO oxidation and relatively low content of precious metals. Abruna *et al.* [123] prepared and studied highly stable and CO-tolerant Pt/$Ti_{0.7}W_{0.3}O_2$ electro-catalyst for proton-exchange-membrane fuel cells. The higher activity for CO oxidation could be attributed to the presence of tungstate and titania in Pt/$Ti_{0.7}W_{0.3}O_2$ relative to electronic effect.

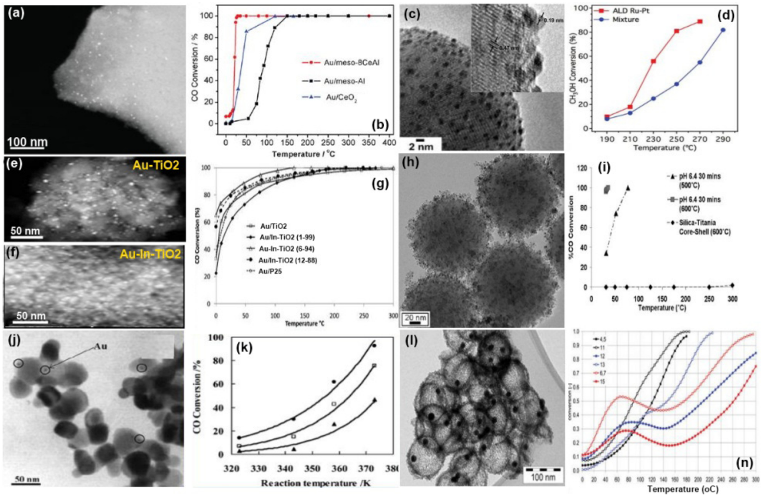

**Figure 9.8** CO oxidation catalytic activity over hybrid metal-oxide nanocrystals: (a) Au/Ce–Al oxide mesoporous materials, (b) CO conversion over Au/meso-CeAl (red line), Au/meso–Al (black line), Au/$CeO_2$ (blue line) at 30°C [114]; (c) bimetallic Ru–Pt particles doped on alumina sphere, (d) Methanol decomposition over the Ru–Pt bimetallic catalyst (red line) and the physical mixture of Ru + Pt monometallic (blue line) catalysts [115]; (e) Au/$TiO_2$, (f) Au/In–$TiO_2$, (g) CO oxidation on the Au/In–$TiO_2$ catalysts and Au/Degussa (P25) reference [116]; (h) Au nanocrystals deposited on silica-titania pebbles and (i) CO conversion of bare silica–titania pebbles, pH = 6.4 gold catalysts without dilution by alumina [117]; (j) Au/$ZrO_2$ nanocrystals and (k) catalytic activity of Au/$ZrO_2$ nanocatalysts [118]; (l) Au@$ZrO_2$ yolk-shell nanocatalysts and (n) CO conversion over Au@$ZrO_2$ yolk-shells [119].

The catalytic activity of Au nanoparticles in Au/$ZrO_2$ for CO oxidation could be greatly improved by reducing the particle size of zirconia nanoparticles (Fig. 9.8j,k). The continuous reduction of the $ZrO_2$ nanoparticles was attributed to Au-oxide contact boundaries and due to the presence of a larger number of oxygen vacancies at the surfaces of smaller $ZrO_2$ nanoparticles [118]. Besides defects have probably the most significant influence on the catalytic properties. The surface termination of dislocations and stacking faults in small 5 nm Au particles in the microstructure of Au–$ZrO_2$ yolk-shell catalysts act as active centers in CO oxidation (Fig. 9.8l,n) [119].

The well dispersion of the tiny bimetallic alloys on the $SiO_2$ supports exhibited the high catalytic activity for CO oxidation. Li *et al.* [124] found that the Au–Ag@$SiO_2$ catalysts are active for CO oxidation even at a reaction temperature as low as –50°C. The turnover frequencies of the Au–Ag/$SiO_2$(3/1) were nearly five times larger than that of the Au/$SiO_2$. The CO oxidation activities followed the order of Au–Ag(3/1)/$SiO_2$ > Au–Ag(1/1)/$SiO_2$ > Au/$TiO_2$ > Au/$SiO_2$ >> Ag/$SiO_2$. This implied that in addition to the particle size effect, the synergetic electronic properties between Au and Ag affected the catalytic performance of Au–Ag alloy catalysts. Pt–Fe/$SiO_2$ and Pt/$SiO_2$ catalysts were tested on the CO oxidation activity and selectivity from the temperature-dependent reaction profile (Fig. 9.9A-D). The Pt/$SiO_2$ catalysts exhibited the weak catalytic activity at room temperature. In contrast, the Pt–Fe/$SiO_2$ catalysts showed a high activity, with almost 100% CO conversion and 100% CO selectivity at room temperature. The high CO conversion (95%) and selectivity (95%) of the Pt–Fe/$SiO_2$ catalysts still remained. Even at very low temperature (200 K), their CO conversion and selectivity maintained about 20%. The Pt–Fe/$SiO_2$ catalysts possessed the concept of the confined coordinately unsaturated ferrous sites, neighboring metal atoms, interface confinement, and coordinately unsaturated low-valent cations that caused the promotion of the high activity and stability in CO oxidation under realistic conditions [120].

Guczi *et al.* [125] have developed the reaction mechanism of CO oxidation on Au/$Fe_2O_3$. They also reported the size effect of Au nanoparticles on the CO catalytic activity, which demonstrated a correlation between Au nanoparticle size, electron structure, and catalytic activity. The valence band density of states of gold nanoparticles changed with decreasing particle size, and the enhancement of activity was attributed to it. It has also been reported that the hydroxyl groups on the surface of the support can create the anchoring site for gold species and stabilize the gold in the

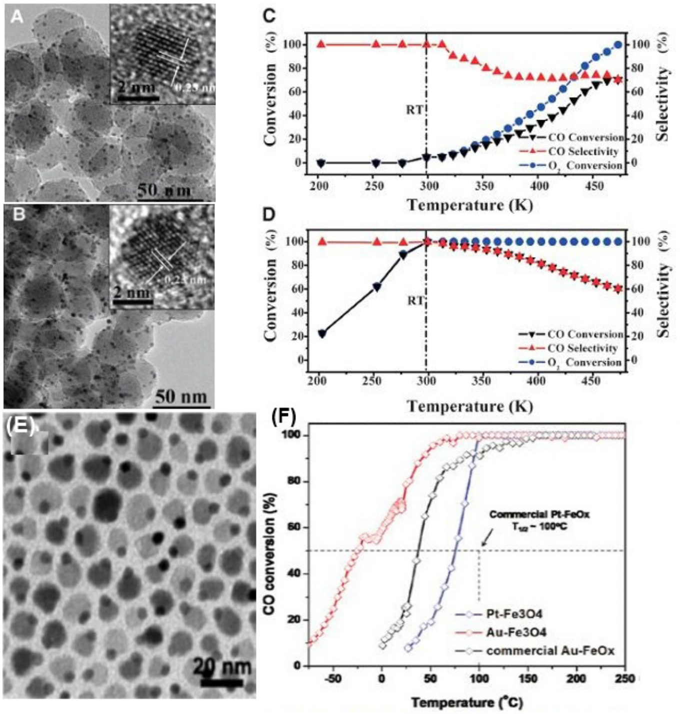

**Figure 9.9** CO oxidation catalytic activity over hybrid metal-oxide nanocrystals: (A) $Pt/SiO_2$, (B) $Pt–Fe/SiO_2$ catalysts, PROX reaction of the (C) $Pt/SiO_2$ and (D) $Pt–Fe/SiO_2$ catalysts [120]; (E) $Au–Fe_3O_4$ dumbell nanocatalysts and (F) CO oxidation conversion light-off curves of $Au–Fe_3O_4$ and $Pt–Fe_3O_4$ NPs, and commercial $Au/Fe_2O_3$ catalyst [121].

dispersed state. If one could prepare an iron-oxide support that has a higher surface area (>200 $m^2/g$), and abundant hydroxyl groups on the surface, it would be a good support for gold in CO oxidation. The noble metal-transition metal-oxide dumbbell ($Au–Fe_3O_4$ and $Pt–Fe_3O_4$) nanohybrids deposited on $SiO_2$ that displayed the enhanced catalytic activity toward CO oxidation compared to their conventional counterparts (Fig. 9.9A,B,C,D) [121]. The $Au–Fe_3O_4$ nanodumbells exhibited a $T_{1/2}$ (half-conversion temperature) of –25°C, compared to a value of 30°C for the conventional $Au/Fe_2O_3$, while the temperature was 67°C for $Pt–Fe_3O_4$ nanodumbells and ~100°C for conventional $Pt/Fe_2O_3$ (Fig. 9.9E,F). The enhanced activities would be not only attributed to the stronger electronic interaction and the larger hetero-junction interface, but also due to their high thermal stability of the metal particles against particle sintering. The effect of pH during the deposition-precipitation on the CO conversion of 3 wt% Au/$Fe_xO_y$ catalysts with surface area of ~400 $m^2g^{-1}$ for low-temperature CO oxidation in humid air under ambient conditions was also investigated by Chen *et al.* [126]. The Au/$Fe_xO_y$ catalyst prepared at pH 9 showed the best performance of CO oxidation. At pHs above, the isoelectric point of the oxide support, adsorption of the negatively charged $[Au(OH)_xCl_{4-x}]^-$ complex decreases rapidly, resulting in a lower gold loading on support. Iwasawa *et al.* [127] prepared highly dispersed gold clusters by impregnating various metal hydroxides with a solution of $[Au_9(PPh_3)_8](NO_3)_3$ solution, and they found that after decomposition, the gold clusters deposited on Mn, Fe, Co, Ni, Cu, and Zn hydroxide were active in the CO oxidation even at sub-ambient temperatures. More detailed studies on the Au/$Fe(OH)_3$ system revealed that after calcination, the catalyst showed extremely high activity. This was ascribed to the stabilization of $[Au(PPh_3)]^+$ species leading to small gold particles. On the other hand, when the complex deposited on $Fe_2O_3$ was decomposed, large gold particles were formed with very low activity in CO oxidation. They also observed $Au^o$ and $Au^{3+}$ species, but no direct correlation was found between the valence state of gold and the catalytic activity. In the later work they identified $Au^+$ species being more active than $Au^o$ particles.

The effect of the encapsulation of the nanohybrid materials on the catalytic activity was also studied [128]. The half-conversion temperature was found to be about 230°C for the Au@$SnO_2$ core/shell supported catalysts and 330°C for the non-encapsulated Au–$SnO_2$ catalyst. The strong interactions between Au and oxide support existed in this encapsulated Au@$SnO_2$ core/shell structure, which might enhance its catalytic performance for CO oxidation. It is expected that the Au@$SnO_2$ core/shell structure had larger interaction areas than the non-encapsulated Au–$SnO_2$ structure, leading to the stronger metal-support interactions. The behavior enhanced the electron transfer from the oxide support to the Au particles and synergetic confinement effect [128]. The Au clusters with sizes below 1 nm supported on $Mg(OH)_2$ were reported to be super-active for the CO oxidation reaction at ultralow temperatures below –70°C [129]. However, the activity for CO oxidation at –70°C was completely lost when the particle size of the gold increased to 3–5 nm after calcinations of this Au/$Mg(OH)_2$ catalyst at 300°C. Cunningham *et al.* claimed that the active state of gold in a Au/$Mg(OH)_2$ catalyst was in the form of icosahedral metal clusters smaller than 1 nm.

## 9.5 Concluding Remarks

This chapter presents the diverse new types of colloidal inorganic hybrid nanomaterials with dumbbell- and core–shell shapes that have been synthesized via various seed-mediated methods over the recent years. The effects of different synthetic surfactant-assisted pathways and the reaction parameters (e.g., time, temperature reactions, and seed-to-precursor ratio) on the heterogeneous growth of the structural-controlled nanohybrids are reviewed.

Different growth mechanisms developed for the formation of hybride dumbbell or core–shell structures from the attachment of two or more nano-components are also expressed. Upon formation of such hybrid nanoparticles, a second challenge arises concerning the understanding of the synergetic properties of the system. The optical and electronic properties of these multifunctional nanostructures often exhibit interesting deviations from their individual components, such as a shift in the plasmon resonance of noble metal nanocrystals or a decrease in the photoluminescence intensity of semiconductor nanocrystals. These changes are attributed to the mutual effects of the electronic properties of the different components.

Multicomponent nanostructures show promise for a number of potential uses due to their multiple functionalities. The ability to form integrated metallic contact points within a multicomponent structure is of great value not only for achieving ohmic electrical contacts but also for utilizing them as anchor points for bottom-up self assembly of the device.

The emergence of the new collective properties of these hybrid systems exhibit novel phenomena making them to be the excellent candidates for their applications in diverse fields, such as biological tagging, medical diagnostics and treatment, optical and electro-optical applications, solar energy harvesting, and more. Although such explorations are still in an early stage, the ability to tune the properties or impart multiple functionalities to hybrid nanomaterials shows high potential for their future inclusion in emerging technologies.

## Acknowledgement

This work was supported by the Natural Sciences and Engineering Research Council of Canada (NSERC) through a strategic grant.

## References

1. Costi, R., A. E. Saunders, and U. Banin, Colloidal hybrid nanostructures: a new type of functional materials. *Angew. Chem. Int. Ed.*, 2010. **49**(29): pp. 4878–4897.
2. Barreca, D., A. Gasparotto, and E. Tondello, Metal/oxide interfaces in inorganic nanosystems: what's going on and what's next? *J. Mater. Chem.*, 2011. **21**: 1648–1654.
3. Buso, D., *et al.*, Gold nanoparticle-doped $TiO_2$ semiconductor thin films: gas sensing properties. *Adv. Funct. Mater.*, 2008. **18**(23): pp. 3843–3849.
4. Mokari, T., *et al.*, Formation of asymmetric one-sided metal-tipped semiconductor nanocrystal dots and rods. *Nat. Mater.*, 2005. **4**(11): pp. 855–863.
5. Banin, U., Nanocrystals: tiny seeds make a big difference. *Nat. Mater.*, 2007. **6**(9): pp. 625–626.
6. Subramanian, V., E. E. Wolf, and P. V. Kamat, Green emission to probe photoinduced charging events in ZnO–Au nanoparticles. Charge distribution and fermi-level equilibration. *J. Phys. Chem. B*, 2003. **107**(30): pp. 7479–7485.
7. Chen, M., and D. W. Goodman, Catalytically active gold: from nanoparticles to ultrathin films. *Acc. Chem. Res.*, 2006. **39**(10): pp. 739–746.
8. Gao, J., H. Gu, and B. Xu, Multifunctional magnetic nanoparticles: design, synthesis, and biomedical applications. *Acc. Chem. Res.*, 2009. **42**(8): pp. 1097–1107.
9. Na, H. B., I. C. Song, and T. Hyeon, Inorganic nanoparticles for mri contrast agents. *Adv. Mater.*, 2009. **21**(21): pp. 2133–2148.
10. Mieszawska, A. J., *et al.*, The synthesis and fabrication of one-dimensional nanoscale heterojunctions. *Small*, 2007. **3**(5): pp. 722–756.
11. Hao, R., *et al.*, Synthesis, functionalization, and biomedical applications of multifunctional magnetic nanoparticles. *Adv. Mater.*, 2010. **22**(25): pp. 2729–2742.
12. Zeng, H., and S. Sun, Syntheses, properties, and potential applications of multicomponent magnetic nanoparticles. *Adv. Funct. Mater.*, 2008. **18**(3): pp. 391–400.

13. Larsen Sarah, C., Nanocatalysts for environmental technology, in Nanotechnology and the Environment. 2004, *Am. Chem. Soc.*, pp. 268–271.
14. Creighton J, R., and M. White J, Transient low-pressure studies of catalytic carbon monoxide oxidation, in Catalysis Under Transient Conditions. 1982, *Am. Chem. Soc.*, pp. 33–58.
15. Peden Charles, H. F., Carbon monoxide oxidation on model single-crystal catalysts, in Surface Science of Catalysis. 1992, *Am. Chem. Soc.*, pp. 143–159.
16. Rethwisch, D. G., and J. A. Dumesic, Adsorptive and catalytic properties of carbon monoxide and carbon dioxide over supported metal oxides, in Catalytic Activation of Carbon Dioxide. 1988, *Am. Chem. Soc.*, pp. 102–122.
17. Leong, W. L., and J. J. Vittal, One-dimensional coordination polymers: complexity and diversity in structures, Properties, and Applications. *Chem. Rev.*, 2011. **111**(2): pp. 688–764.
18. Skrabalak, S. E., and Y. Xia, Pushing nanocrystal synthesis toward nanomanufacturing. *ACS Nano*, 2009. **3**(1): pp. 10–15.
19. Burda, C., *et al.*, Chemistry and properties of nanocrystals of different shapes. *Chemical Reviews*, 2005. **105**(4): pp. 1025–1102.
20. Grassian Vicki, H., Size-dependent properties and surface chemistry of oxide-based nanomaterials in environmental processes, in Nanoscale Materials in Chemistry: Environmental Applications. 2010, *Am. Chem. Soc.*, pp. 15–33.
21. El-Sayed, M. A., Small is different: shape-, size-, and composition-dependent properties of some colloidal semiconductor nanocrystals. *Acc. Chem. Res.*, 2004. **37**(5): pp. 326–333.
22. El-Sayed, M. A., Some interesting properties of metals confined in time and nanometer space of different shapes. *Acc. Chem. Res.*, 2001. **34**(4): pp. 257–264.
23. Tisdale, W. A., *et al.*, Hot-electron transfer from semiconductor nanocrystals. *Science*, 2010. **328**(5985): pp. 1543–1547.
24. Carbone, L. and P.D. Cozzoli, Colloidal heterostructured nano-crystals: synthesis and growth mechanisms. *Nano Today*, 2010. **5**(5): pp. 449–493.
25. Yu, H., *et al.*, Dumbbell-like bifunctional Au–$Fe_3O_4$ nanoparticles. *Nano Lett.*, 2005. **5**(2): pp. 379–382.
26. Xu, C., *et al.*, Au–$Fe_3O_4$ dumbbell nanoparticles as dual-functional probes. *Angew. Chem. Int. Ed.*, 2008. **47**(1): pp. 173–176.

27. Lee, Y., *et al.*, Synthetic tuning of the catalytic properties of Au–$Fe_3O_4$ nanoparticles. *Angew. Chem. Int. Ed.*, 2010. **49**(7): pp. 1271–1274.
28. Shevchenko, E. V., *et al.*, Gold/iron oxide core/hollow-shell nanoparticles. *Adv. Mater.*, 2008. **20**(22): pp. 4323–4329.
29. Levin, C. S., *et al.*, Magnetic–plasmonic core–shell nanoparticles. *ACS Nano*, 2009. **3**(6): pp. 1379–1388.
30. Choi, S.-H., *et al.*, Simple and generalized synthesis of oxide–metal heterostructured nanoparticles and their applications in multimodal biomedical probes. *J. Am. Chem. Soc.*, 2008. **130**(46): pp. 15573–15580.
31. Bao, J., *et al.*, Bifunctional Au–$Fe_3O_4$ nanoparticles for protein separation. *ACS Nano*, 2007. **1**(4): pp. 293–298.
32. Xu, Z., Y. Hou, and S. Sun, Magnetic core/shell $Fe_3O_4$/Au and $Fe_3O_4$/Au/Ag nanoparticles with tunable plasmonic properties. *J. Am. Chem. Soc.*, 2007. **129**(28): pp. 8698–8699.
33. Zhang, J., *et al.*, A general approach to fabricate diverse noble-metal (Au, Pt, Ag, Pt/Au)/$Fe_2O_3$ hybrid nanomaterials. *Chem. Eur. J.*, 2010. **16**(27): pp. 8108–8116.
34. Zeng, H., *et al.*, Bimagnetic core/shell FePt/$Fe_3O_4$ nanoparticles. *Nano Lett.*, 2003. **4**(1): pp. 187–190.
35. Mazumder, V., *et al.*, Core/shell Pd/FePt nanoparticles as an active and durable catalyst for the oxygen reduction reaction. *J. Am. Chem. Soc.*, 2010. **132**(23): pp. 7848–7849.
36. Kuo, C.-H., T.-E. Hua, and M. H. Huang, Au nanocrystal-directed growth of Au–$Cu_2O$ Core–shell heterostructures with precise morphological control. *J. Am. Chem. Soc.*, 2009. **131**(49): pp. 17871–17878.
37. Wang, D., and Y. Li, One-pot protocol for au-based hybrid magnetic nanostructures via a noble-metal-induced reduction process. *J. Am. Chem. Soc.*, 2010. **132**(18): pp. 6280–6281.
38. Yang, Y., *et al.*, Diffusion-facilitated fabrication of gold-decorated $Zn_2SiO_4$ nanotubes by a one-step solid-state reaction. *Angew. Chem.*, 2010. **122**(8): pp. 1484–1488.
39. Cargnello, M., *et al.*, Synthesis of dispersible Pd@$CeO_2$ core–shell nanostructures by self-assembly. *J. Am. Chem. Soc.*, 2009. **132**(4): pp. 1402–1409.
40. Mason, G., An experimental determination of the stable length of cylindrical liquid bubbles. *J. Colloid. Interface Sci.*, 1970. **32**(1): pp. 172–176.

41. Chen, P.-H., *et al*., Direct observation of Au/$Ga_2O_3$ peapodded nanowires and their plasmonic behaviors. *Nano Lett*., 2010. **10**(9): pp. 3267–3271.

42. Cheng, C., *et al*., Hierarchical assembly of ZnO nanostructures on $SnO_2$ backbone nanowires: low-temperature hydrothermal preparation and optical properties. *ACS Nano*, 2009. **3**(10): pp. 3069–3076.

43. Guerrero-Martínez, A., J. Pérez-Juste, and L. M. Liz-Marzán, Recent progress on silica coating of nanoparticles and related nanomaterials. *Adv. Mater*., 2010. **22**(11): pp. 1182–1195.

44. Li, X., *et al*., Multifunctional Au-coated $TiO_2$ nanotube arrays as recyclable SERS substrates for multifold organic pollutants detection. *Adv. Funct. Mater*., 2010. **20**(17): pp. 2815–2824.

45. Wang, C., *et al*., Platinum-nanoparticle-modified $TiO_2$ nanowires with enhanced photocatalytic property. *ACS Appl. Mater. Interfaces*, 2010. **2**(11): pp. 3373–3377.

46. Sahoo, J. K., *et al*., Reversible self-assembly of metal chalcogenide/metal oxide nanostructures based on pearson hardness. *Angew. Chem. Int. Ed*., 2010. **49**(41): pp. 7578–7582.

47. Gong, K., D. Su, and R. R. Adzic, Platinum-monolayer shell on $AuNi_{0.5}Fe$ nanoparticle core electrocatalyst with high activity and stability for the oxygen reduction reaction. *J. Am. Chem. Soc*., 2010. **132**(41): pp. 14364–14366.

48. Ma, Y., *et al*., Au@Ag core−shell nanocubes with finely tuned and well-controlled sizes, shell thicknesses, and optical properties. *ACS Nano*, 2010. **4**(11): pp. 6725–6734.

49. Wen, T., and K. M. Krishnan, Thermal stability and morphological transformations of Aucore−Coshell nanocrucibles. *J. Phys. Chem. C*, 2010. **114**(35): pp. 14838–14842.

50. Mokari, T., *et al*., Selective growth of metal tips onto semiconductor quantum rods and tetrapods. *Science*, 2004. **304**(5678): pp. 1787–1790.

51. Menagen, G., *et al*., Au growth on semiconductor nanorods: photoinduced versus thermal growth mechanisms. *J. Am. Chem. Soc*., 2009. **131**(47): pp. 17406–17411.

52. Kudera, S., *et al*., Selective growth of PbSe on one or both tips of colloidal semiconductor nanorods. *Nano Lett*., 2005. **5**(3): pp. 445–449.

53. Meyns, M., *et al*., Growth and reductive transformation of a gold shell around pyramidal cadmium selenide nanocrystals. *J. Mater. Chem*., 2010. **20**(47): pp. 10602–10605.

54. Kwon, K.-W., and M. Shim, $\gamma$-$Fe_2O_3$/II−VI sulfide nanocrystal heterojunctions. *J. Am. Chem. Soc*., 2005. **127**(29): pp. 10269–10275.

55. Macdonald, J. E., *et al*., Hybrid nanoscale inorganic cages. *Nat. Mater.*, 2010. **9**(10): pp. 810–815.

56. Myung, Y., *et al*., Composition-tuned ZnO–CdSSe core–shell nanowire arrays. *ACS Nano*, 2010. **4**(7): pp. 3789–3800.

57. Lee, J.-S., *et al*., “Magnet-in-the-semiconductor” FePt–PbS and FePt–PbSe nanostructures: magnetic properties, charge transport, and magnetoresistance. *J. Am. Chem. Soc.*, 2010. **132**(18): pp. 6382–6391.

58. Liu, N., B. S. Prall, and V. I. Klimov, Hybrid gold/silica/nanocrystal-quantum-dot superstructures: synthesis and analysis of semiconductor–metal interactions. *J. Am. Chem. Soc.*, 2006. **128**(48): pp. 15362–15363.

59. Chakrabortty, S., *et al*., Asymmetric dumbbells from selective deposition of metals on seeded semiconductor nanorods. *Angew. Chem. Int. Ed.*, 2010. **49**(16): pp. 2888–2892.

60. Huang, S., *et al*., Chemical synthesis, structure characterization, and optical properties of hollow $PbS_x$–solid Au heterodimer nanostructures. *Chem. Euro. J.*, 2010. **16**(20): pp. 5920–5926.

61. Liu, M., and P. Guyot-Sionnest, Preparation and optical properties of silver chalcogenide coated gold nanorods. *J. Mater. Chem.*, 2006. **16**(40): pp. 3942–3945.

62. Tian, Z.-Q., *et al*., Core/Shell structured noble metal (alloy)/cadmium selenide nanocrystals. *Chem. Mater.*, 2009. **21**(14): pp. 3039–3041.

63. Lee, J.-S., E. V. Shevchenko, and D. V. Talapin, Au–PbS core–shell nanocrystals: plasmonic absorption enhancement and electrical doping via intra-particle charge transfer. *J. Am. Chem. Soc.*, 2008. **130**(30): pp. 9673–9675.

64. Luo, Y., and L.-W. Wang, Electronic structures of the CdSe/CdS core–shell nanorods. *ACS Nano*, 2009. **4**(1): pp. 91–98.

65. Xu, J., *et al*., Large-scale synthesis and phase transformation of CuSe, $CuInSe_2$, and $CuInSe_2/CuInS_2$ core/shell nanowire bundles. *ACS Nano*, 2010. **4**(4): pp. 1845–1850.

66. Lee, D.C., *et al*., Infrared-active heterostructured nanocrystals with ultralong carrier lifetimes. *J. Am. Chem. Soc.*, 2010. **132**(29): pp. 9960–9962.

67. Ferrando, R., J. Jellinek, and R. L. Johnston, Nanoalloys: from theory to applications of alloy clusters and nanoparticles. *Chem. Rev.*, 2008. **108**(3): pp. 845–910.

68. Rodriguez-Gonzalez, B., *et al*., Multishell bimetallic AuAg nanoparticles: synthesis, structure and optical properties. *J. Mater. Chem.*, 2005. **15**(17): pp. 1755–1759.

69. Xiang, Y., *et al.*, Formation of rectangularly shaped Pd/Au bimetallic nanorods: evidence for competing growth of the pd shell between the {110} and {100} side facets of au nanorods. *Nano Lett.*, 2006. **6**(10): pp. 2290–2294.

70. Ni, W., *et al.*, Tailoring longitudinal surface plasmon wavelengths, scattering and absorption cross sections of gold nanorods. *ACS Nano*, 2008. **2**(4): pp. 677–686.

71. Park, K., and R. A. Vaia, Synthesis of complex Au/Ag nanorods by controlled overgrowth. *Adv. Mater.*, 2008. **20**(20): pp. 3882–3886.

72. Carbó-Argibay, E., *et al.*, The crystalline structure of gold nanorods revisited: evidence for higher-index lateral facets. *Angew. Chem.*, 2010. **122**(49): pp. 9587–9590.

73. Cho, E. C., P. H. C. Camargo, and Y. Xia, Synthesis and characterization of noble-metal nanostructures containing gold nanorods in the center. *Adv. Mater.*, 2010. **22**(6): pp. 744–748.

74. Okuno, Y., *et al.*, Rapid formation of silver shells on gold nanorods in a micellar solution of hexadecyltrimethylammonium chloride. *Chem. Lett.*, 2009. **38**(1): pp. 60–61.

75. Okuno, Y., *et al.*, Uniform and controllable preparation of Au–Ag core–shell nanorods using anisotropic silver shell formation on gold nanorods. *Nanoscale*, 2010. **2**(8): pp. 1489–1493.

76. Fernanda Cardinal, M., *et al.*, Modulation of localized surface plasmons and sers response in gold dumbbells through silver coating. *J. Phys. Chem. C*, 2010. **114**(23): pp. 10417–10423.

77. Gonzalez, C. M., Y. Liu, and J. C. Scaiano, Photochemical strategies for the facile synthesis of gold–silver alloy and core–shell bimetallic nanoparticles. *J. Phys. Chem. C*, 2009. **113**(27): pp. 11861–11867.

78. Yoo, H., *et al.*, Core–Shell triangular bifrustums. *Nano Lett.*, 2009. **9**(8): pp. 3038–3041.

79. Lim, B., *et al.*, Twin-induced growth of palladium–platinum alloy nanocrystals. *Angew. Chem. Int. Ed.*, 2009. **48**(34): pp. 6304–6308.

80. Jiang, M., *et al.*, Epitaxial overgrowth of platinum on palladium nanocrystals. *Nanoscale*, 2010. **2**(11): pp. 2406–2411.

81. Fan, F.-R., *et al.*, Epitaxial growth of heterogeneous metal nanocrystals: from gold nano-octahedra to palladium and silver nanocubes. *J. Am. Chem. Soc.*, 2008. **130**(22): pp. 6949–6951.

82. Lim, B., *et al.*, Synthesis of Pd–Au bimetallic nanocrystals via controlled overgrowth. *J. Am. Chem. Soc.*, 2010. **132**(8): pp. 2506–2507.

83. Lu, C.-L., *et al*., Au nanocube-directed fabrication of Au–Pd core–shell nanocrystals with tetrahexahedral, concave octahedral, and octahedral structures and their electrocatalytic activity. *J. Am. Chem. Soc.*, 2010. **132**(41): pp. 14546–14553.
84. Song, S., *et al*., Colloidal noble-metal and bimetallic alloy nanocrystals: a general synthetic method and their catalytic hydrogenation properties. *Chem. Euro. J.*, 2010. **16**(21): pp. 6251–6256.
85. Yuan, Q., J. Zhuang, and X. Wang, Single-phase aqueous approach toward Pd sub-10 nm nanocubes and Pd–Pt heterostructured ultrathin nanowires. *Chem. Commun.*, 2009(43): pp. 6613–6615.
86. Lim, B., *et al*., Pd–Pt bimetallic nanodendrites with high activity for oxygen reduction. *Science*, 2009. **324**(5932): pp. 1302–1305.
87. Habas, S. E., *et al*., Shaping binary metal nanocrystals through epitaxial seeded growth. *Nat. Mater.*, 2007. **6**(9): pp. 692–697.
88. Ataee-Esfahani, H., *et al*., Synthesis of bimetallic Au@Pt nanoparticles with Au core and nanostructured Pt shell toward highly active electrocatalysts. *Chem. Mater.*, 2010. **22**(23): pp. 6310–6318.
89. Lu, Y., *et al*., *In situ* growth of catalytic active Au–Pt bimetallic nanorods in thermoresponsive core–shell microgels. *ACS Nano*, 2010. **4**(12): pp. 7078–7086.
90. Alayoglu, S., *et al*., Ru–Pt core–shell nanoparticles for preferential oxidation of carbon monoxide in hydrogen. *Nat. Mater.*, 2008. **7**(4): pp. 333–338.
91. Skrabalak, S. E., *et al*., Gold nanocages: synthesis, properties, and applications. *Acc. Chem. Res.*, 2008. **41**(12): pp. 1587–1595.
92. Pang, M., J. Hu, and H. C. Zeng, Synthesis, morphological control, and antibacterial properties of hollow/solid $Ag_2S$/Ag heterodimers. *J. Am. Chem. Soc.*, 2010. **132**(31): pp. 10771–10785.
93. Glaspell, G., L. Fuoco, and M. S. El-Shall, Microwave synthesis of supported Au and Pd nanoparticle catalysts for CO oxidation. *J. Phys. Chem. B*, 2005. **109**(37): pp. 17350–17355.
94. Huang, X.-S., *et al*., Morphology effects of nanoscale ceria on the activity of Au/$CeO_2$ catalysts for low-temperature CO oxidation. *Appl. Catal. B: Environmental*, 2009. **90**(1–2): pp. 224–232.
95. Andreeva, D., *et al*., Gold based catalysts on ceria and ceria-alumina for WGS reaction (WGS Gold catalysts). *Top Catal.*, 2007. **44**(1): pp. 173–182.
96. Huang, P. X., *et al*., $CeO_2$ nanorods and gold nanocrystals supported on $CeO_2$ nanorods as catalyst. *J. Phys. Chem. B*, 2005. **109**(41): pp. 19169–19174.

97. Guzman, J., S. Carrettin, and A. Corma, Spectroscopic evidence for the supply of reactive oxygen during CO oxidation catalyzed by gold supported on nanocrystalline $CeO_2$. *J. Am. Chem. Soc.*, 2005. **127**(10): pp. 3286–3287.
98. Venezia, A. M., *et al.*, Relationship between structure and CO oxidation activity of ceria-supported gold catalysts. *J. Phys. Chem. B*, 2005. **109**(7): pp. 2821–2827.
99. Cargnello, M., *et al.*, Active and stable embedded Au@$CeO_2$ catalysts for preferential oxidation of CO. *Chem. Mater.*, 2010. **22**(14): pp. 4335–4345.
100. Camellone, M. F., and S. Fabris, Reaction mechanisms for the CO oxidation on Au/$CeO_2$ catalysts: activity of substitutional $Au^{3+}$/$Au^+$ cations and deactivation of supported $Au^+$ adatoms. *J. Am. Chem. Soc.*, 2009. **131**(30): pp. 10473–10483.
101. Han, M., *et al.*, Preparation of highly active, low Au-loaded, Au/$CeO_2$ nanoparticle catalysts that promote CO oxidation at ambient temperatures. *J. Phys. Chem. C*, 2009. **114**(2): pp. 793–798.
102. Hinokuma, S., *et al.*, Metallic Pd nanoparticles formed by Pd–O–Ce interaction: a reason for sintering-induced activation for CO oxidation. *Chem. Mater.*, 2010. **22**(22): pp. 6183–6190.
103. Boronin, A. I., *et al.*, Investigation of palladium interaction with cerium oxide and its state in catalysts for low-temperature CO oxidation. *Catal. Today*, 2009. **144**(3–4): pp. 201–211.
104. Huang, P. X., *et al.*, Praseodymium hydroxide and oxide nanorods and Au/Pr6O11 nanorod catalysts for CO oxidation. *J. Phys. Chem. B*, 2006. **110**(4): pp. 1614–1620.
105. Abdelsayed, V., *et al.*, Microwave synthesis of bimetallic nanoalloys and CO oxidation on ceria-supported nanoalloys. *Chem. Mater.*, 2009. **21**(13): pp. 2825–2834.
106. Gamarra, D., *et al.*, Selective CO oxidation in excess $H_2$ over copper–ceria catalysts: identification of active entities/species. *J. Am. Chem. Soc.*, 2007. **129**(40): pp. 12064–12065.
107. Hornés, A., *et al.*, Inverse $CeO_2$/CuO catalyst as an alternative to classical direct configurations for preferential oxidation of CO in hydrogen-rich stream. *J. Am. Chem. Soc.*, 2009. **132**(1): pp. 34–35.
108. Hernández, W. Y., *et al.*, Synthesis and characterization of $Ce_{1-x}Eu_xO_{2-x/2}$ mixed oxides and their catalytic activities for CO oxidation. *J. Phys. Chem. C*, 2009. **113**(14): pp. 5629–5635.

109. Daté, M., *et al*., Performance of Au/$TiO_2$ catalyst under ambient conditions. *Catal*. *Today*, 2002. **72**(1–2): pp. 89–94.

110. Valden, M., X. Lai, and D. W. Goodman, Onset of catalytic activity of gold clusters on titania with the appearance of nonmetallic properties. *Science*, 1998. **281**(5383): pp. 1647–1650.

111. Rolison, D. R., Catalytic Nanoarchitectures — the importance of nothing and the unimportance of periodicity. *Science*, 2003. **299**(5613): pp. 1698–1701.

112. Moreau, F., and G. C. Bond, Preparation and reactivation of Au/$TiO_2$ catalysts. *Catal*. *Today*, 2007. **122**(3–4): pp. 260–265.

113. Gómez-Cortés, A., *et al*., Au–Ir/$TiO_2$ prepared by deposition precipitation with urea: improved activity and stability in CO oxidation. *J*. *Phys*. *Chem*. *C*, 2009. **113**(22): pp. 9710–9720.

114. Yuan, Q., *et al*., Ceria nanocatalysts: homogeneously dispersed ceria nanocatalyst stabilized with ordered mesoporous alumina (Adv. Mater. 13/2010). *Adv*. *Mater*., 2010. **22**(13): pp. 1475–1478.

115. Christensen, S. T., *et al*., Supported Ru–Pt bimetallic nanoparticle catalysts prepared by atomic layer deposition. *Nano Letters*, 2010. **10**(8): pp. 3047–3051.

116. Rodríguez-González, V., *et al*., Low-temperature CO oxidation and long-term stability of Au/$In_2O_3$–$TiO_2$ catalysts. *J*. *Phys*. *Chemy C*, 2009. **113**(20): pp. 8911–8917.

117. Lim, S. H., *et al*., Robust gold-decorated silica–titania pebbles for low-temperature CO catalytic oxidation. *Langmuir*, 2009. **25**(16): pp. 9480–9486.

118. Zhang, X., H. Wang, and B.-Q. Xu, Remarkable nanosize effect of zirconia in Au/$ZrO_2$ catalyst for CO oxidation. *J*. *Phys*. *Chem*. *B*, 2005. **109**(19): pp. 9678–9683.

119. Pandey, A. D., *et al*., Influence of the microstructure of gold–zirconia yolk–shell catalysts on the CO oxidation activity. *J*. *Phys*. *Chem*. *C*, 2010. **114**(45): pp. 19386–19394.

120. Fu, Q., *et al*., Interface-confined ferrous centers for catalytic oxidation. *Science*, 2010. **328**(5982): pp. 1141–1144.

121. Wang, C., *et al*., A general approach to noble metal–metal oxide dumbbell nanoparticles and their catalytic application for CO oxidation. *Chem*. *Mater*., 2010. **22**(10): pp. 3277–3282.

122. Saravanan, G., *et al*., $Pt_3Ti$ nanoparticles: fine dispersion on $SiO_2$ supports, enhanced catalytic CO oxidation, and chemical stability at elevated temperatures. *Langmuir*, 2010. **26**(13): pp. 11446–11451.

123. Wang, D., *et al.*, Highly stable and CO-tolerant Pt/$Ti_{0.7}W_{0.3}O_2$ electrocatalyst for proton-exchange membrane fuel cells. *J. Am. Chem. Soc.*, 2010. **132**(30): pp. 10218–10220.

124. Liu, X., *et al.*, Synthesis of thermally stable and highly active bimetallic Au–Ag nanoparticles on inert supports. *Chem. Mater.*, 2008. **21**(2): pp. 410–418.

125. Horváth, D., L. Toth, and L. Guczi, Gold nanoparticles: effect of treatment on structure and catalytic activity of Au/$Fe_3O_4$ catalyst prepared by co-precipitation. *Catal. Lett.*, 2000. **67**(2): pp. 117–128.

126. Lin, H.-Y., and Y.-W. Chen, Low-temperature CO oxidation on Au/$Fe_xO_y$ catalysts. *Ind. Eng. Chem. Res.*, 2005. **44**(13): pp. 4569–4576.

127. Kozlova, A. P., *et al.*, Study of gold species in iron-oxide-supported gold catalysts derived from gold-phosphine complex $Au(PPh_3)(NO_3)$ and As-precipitated wet $Fe(OH)_3$. *J. Catal.*, 1999. **181**(1): pp. 37–48.

128. Yu, K., *et al.*, High-temperature-stable Au@$SnO_2$ core/shell supported catalyst for CO oxidation. *J. Phys. Chem. C*, 2008. **112**(7): pp. 2244–2247.

129. Jia, C.-J., *et al.*, Very low temperature CO oxidation over colloidally deposited gold nanoparticles on $Mg(OH)_2$ and MgO. *J. Am. Chem. Soc.*, 2010. **132**(5): pp. 1520–1522.